

Modelling CO₂ adsorption in a thin discrete packing

Authors : Michael Wray, Farida Amrouche and Farid Aiouache*
Lancaster University, School of engineering, LA1 4YR, UK

*Corresponding author: e-mail: f.aiouache@lancaster.a.cuk

Abstract:

Local dynamics of CO₂ adsorption in a discrete packing contained in a thin tube was assessed by 3D modelling. Thin tube packed bed adsorbers are currently used over tube structures in thermochemical energy storage systems and atmospheric revitalization of confined spaces. Driven by interplays between key factors such as the exothermicity and the fluid flow, the advective transport was found less effective than the diffusive one on the breakthrough trends of CO₂ which displayed significant concentration gradients at both inter- and intra-particle scales. The lack of angular symmetry inside the particles by the reduction in resistance to mass transfer in area of solid particles exposed to high velocities led to greater convective transports from bulk of the gaseous phase to the pores. The result of the modelling agreed with the experimental data obtained at the exit of the adsorber, helping reduction in reliance on the empirical dispersion models used in the one-dimensional modelling.

Introduction

With the current environmental concerns and restrictions being placed on emissions, the reduction of anthropogenic pollutants stands as an important potential solution. The Paris agreement has set an ambitious target to mitigate effects of global warming by a reduction of 45% by 2030 in greenhouse (GHG) emissions to reach net zero by 2050¹. CO₂ gas however, as the largest contributor to the production of these, is still exhibiting an alarming increase of its global concentration. An effective prevention or reduction of its release to the atmosphere will be a strong step in the direction of mitigating GHG effects. An area of focus within the CO₂ reduction strategies is the capture through adsorption in packed bed adsorbers (PBA). These beds make use of stationary solid particles held within a tubular vessel that captures CO₂ by means of a physical adsorption, via an ion–dipole interaction with the CO₂ in a linear orientation, from fluid streams passing through. The process is one of mass transfer principles and relies on good surface of capture and high selectivity to CO₂ of typical gas mixtures. Fundamental understanding of the local adsorption is crucial to design and effectively operate the PBA devices.

An approach to engineering solutions involves a number of approximations (e.g. an averaging into single dimensional (1D) and two-dimensional (2D) models) which are often specifically tailored to individual operational cases. This approach to engineering design, which is adopted for the generation of key adsorption design parameters, such as the breakthrough curves and the adsorption times, could be complemented by description of the local phenomena taking place at the intra- and inter-particle levels of PBA. The case of the adsorption of CO₂ is worth investigation as it uses microporous materials of large surface area, and thus the relevance of mass transfer in the pores cannot be ignored. Due to interactions of mass transfer and fluid flow, the adsorption and/or desorption cycles are typically designed by use of approximation models such as the linear driving force (LDF) models associated with breakthrough curves at

the exit of the PBA²⁻⁴. The LDF models include spatially averaged information on surface adsorption, mass and heat transfers inside and outside the solid adsorbent. While this term is used variably by the authors, LDF applies to the surface of adsorption by assuming an average concentration within the particles and a uniform temperature. This lumping approach of phases characteristics is associated with the models describing the local rates of adsorption and isotherms at the particle level that are often lost in the final solutions. Such approach might become insufficient for tube bundle types adsorbers of low aspect ratio (AR) of tube to particle diameter of PBA with wall effects on porosity of the bed, leading to non-uniformity of flow, mass and heat. The tube bundle types adsorbers are seeing interests in applications to the thermochemical energy storage, atmospheric revitalization, and fine chemistry^{5,6}, anticipating additional knowledge on management of non-uniform mixing of flow. Typically used for applications of adsorption processes to manage impact of the exothermicity and mitigate non-isothermal operations, low AR packed tube bundles or single packed beds are adapted to applications such as the direct air capture, air drying, energy storage, laboratory scale gas separation and chromatographic analysis where the operated flow rates are generally of moderate values⁷⁻⁹.

One of the keys when carrying out three-dimensional (3D) modelling is the reduced use of lumped models of averaged mass and heat transfer coefficients between the adsorbents and fluid in the PBA. Siriwardane et al.⁷ investigated the adsorption of water vapour in a discrete structure using the Lattice Boltzmann Method. Interesting non-symmetric phenomena of concentration trends in the PBA were observed at pore scale, which were caused by an uneven distribution between particles of the macro-pore voids.¹⁰ Symmetrical trends around the central axis were however observed, despite uneven void concentrations, when slow uptakes in the solid phase occurred. Further observations were extended to non-uniform radial gradients of temperature in regions of low to stagnant flow, affecting breakthrough profiles and times.

Literature is richer however with models of adsorption based on the LDF models or deactivation models to account for the contribution of mass transfer to the kinetics of adsorption¹¹⁻¹². These models relied on assumption of homogenous temperature in the beads while model parameters responsible of flow dispersion such as the transfer coefficients were estimated by a fitting approach of data from laboratory experiments. For instance, Dantas et al.¹³ investigated by process modelling the dual adsorption of CO₂ and N₂ inside a PBA of zeolite 13X. The model was based upon the LDF approach and included the thermal effects and allowed access to rate of adsorption inside the particle adsorber by assuming the geometrical profiles of concentration and temperature occurring in large size PBA. In case of low AR however, non-axially symmetric profiles of concentration and temperature are anticipated due to velocity heterogeneity which justifies use of complementary information on the PBA for 1D models¹¹. Knox et al.² recommended use of local data, instead of exit data, due to front-sharpening patterns of concentration due the axial dispersion, typically considered constant along the PBA 1D models .

The work undertaken herein is focused on local behaviour of CO₂ adsorption inside a PBA of zeolite using the configuration of a discrete packing. Nanoporous Zeolites were selected as they exhibit a physical type of adsorption of CO₂ and N₂ with reduced relevance of kinetics regime of surface adsorption with reference to the associated transport phenomena of heat and mass inside and around the porous surfaces¹⁴. Zeolites are one of the favoured structures for the post-combustion application due to the structured crystalline framework and the controlled pore size variations¹⁵. The crystalline framework offers both chemical and size limitations on adsorbing species, and this means selectivity and capacity, particularly at high temperature or in presence of contaminants such as water vapours, can be tuned at user's preference¹⁶.

An issue with zeolites in the application of CO₂ adsorption is the low selectivity between other components in gaseous streams (N₂, H₂O etc). As well as this, and similarly to other physical

adsorption type materials, the capacities are sensibly reduced at increased temperature, which may pose problems in flue gas treatments. Siriwardane et al.⁷ tested various zeolites for carbon capture from flue gas, e.g. zeolite 13 X and UOP – WEG – 592 and noted reduction in adsorption capacity in presence of water vapour. Liquid impregnated solid sorbents and other surface coating are among techniques for tuning the hydrophilicity of zeolite 13 X that allow an efficient physisorption of CO₂ via Van der Waals forces and hydrogen bonding mechanism^{8,9}.

The kinetics of adsorption was recurrently found to be dominated by the macropore type of diffusion^{17,18}, fitting well the Knudsen diffusion model. Silva et al.¹⁹ however have shown some microporous (i.e., inside the crystals) type relevance of the diffusion model using various geometries of zeolites 13X and range of operating temperature. Unlike the micropore diffusion, the macropore one is known to be sensitive to adsorber geometry and size, pressure drops and thus overall flow dynamics. The visualisation of interaction of flow dynamics and diffusion in the beds would help understanding overall adsorption kinetics in 13X beads. In fact, the diffusion time (ratio of diffusivity and pore size) is affected by pore size which is greater in the macropores but also by the length of these which is smaller in the micropores, leading to competition of the two types of diffusivities based on pellet size and geometry.

The approach proposed herein uses computational fluid dynamics (CFD) for a 3D flow model in a heterogeneous gas-solid system of porous media of assembled particles built by the discrete element method (DEM). The results are assessed by considering impact of adsorption characteristics on the breakthrough data, resulting from the internal flow dynamics.

1. Model development

1.1 Building a random packed bed

The assembly of a typical AR of tube to particle ratio in this study was of 5 and generated 1194 spherical particles using the DEM. The number of particles allowed design of a packing bed of approximately 30 cm height in a cylindrical tube of 2.5 cm internal diameter (particle diameter size of 0.5 cm). The modelling of particles falling into the cylinder was carried out by using a code written in the embedded FISH programming language of the Particle Flow Code PFC^{3D} (Itasca Ltd) and more details on building the code are available in previous works^{20,21}. Once the DEM process converged to a point of particle stability, an output 3D matrix was produced that listed a series of particle coordinates. These coordinates were then converted into a CAD format that was compatible with the CFD package, COMSOL Multiphysics' interface. The geometry in COMSOL could then be observed as a series of suspended spheres, and so a cylinder was built to define the vessel holding the particles. The geometry was then ready for discretisation as shown **Figure 1(a)**.

1.2 Structure validation

The relevance of observation of the 3D structure in comparison with the 2D or 1D structures was assessed through analysis of the bed porosity distribution. The later was then validated by literature models^{22,23}. After the discretisation of the volume matrix into 3D unstructured mesh of averaged spatial resolution of at least 25 elements per particle diameter, the size of particles was reduced by about 0.4% to minimize impact of skewed elements at contact points of the particles^{20,21}. The characteristics of the meshes were constantly refined until reaching pressure drops results which were independent of mesh size. The elements of volume, boundary layer thickness at solid-to-gas, element sizes and expansion rates were constantly refined until

reaching results of pressure drops at reduced mesh size effect for a reasonable computation time (see discretisation assessment in the supporting information). A space resolution of 0.5 x 0.5 x 0.5 mm³ was found satisfactory to observe the variation of local porosity ϕ_{3D} at reduced distortions, particularly in the regions of low meshing resolution.

Thus, the 3D data of the volume matrix were averaged along the angular coordinate θ into a 2D surface bed porosity map ϕ_{2D} (Equation 1) and along radial r and axial h coordinates into overall bed porosity ϕ_{ave} (Equations 2 and 3), allowing access to local data of bed porosity and prediction of flow trends which otherwise would be challenging to read using the 3D assembly.

$$\phi_{2D}(r, h) = \frac{\int_0^{2\pi} \phi_{3D}(r, h, \theta) \theta d\theta}{\int_0^{2\pi} \theta d\theta} \quad (1)$$

$$\phi_{1D}(r) = \frac{\int_0^L \int_0^{2\pi} \phi_{3D}(r, h, \theta) \theta h d\theta dh}{\int_0^L \int_0^{2\pi} \theta h d\theta dh} \quad (2)$$

$$\phi_{ave} = \frac{\int_0^R \int_0^L \int_0^{2\pi} \phi_{3D}(r, h, \theta) \theta h r d\theta dh dr}{\int_0^R \int_0^L \int_0^{2\pi} \theta h r d\theta dh dr} \quad (3)$$

where r , h and θ are the cylindrical coordinates of bed porosity. The bed porosity map in **Figure 1(b)** confirms the large bed porosity distribution in the vicinity of the wall, which is a characteristic of packed beds of low AR, and the progressive reduction towards the centre of the PBA (**Figure 1(c)**). Overall bed porosity ϕ_{ave} showed average deviations of 6.1% from the models²¹. This deviation could be driven by the management of skewed contact points of particles. It is interesting to note that the averaged trends of bed porosity did not capture local arrangements of the structure of the PBA along the angular direction θ as exhibited by the 3D structure, demonstrating relevance of the 3D modelling of CO₂ in comparison with classical D and 2D models.

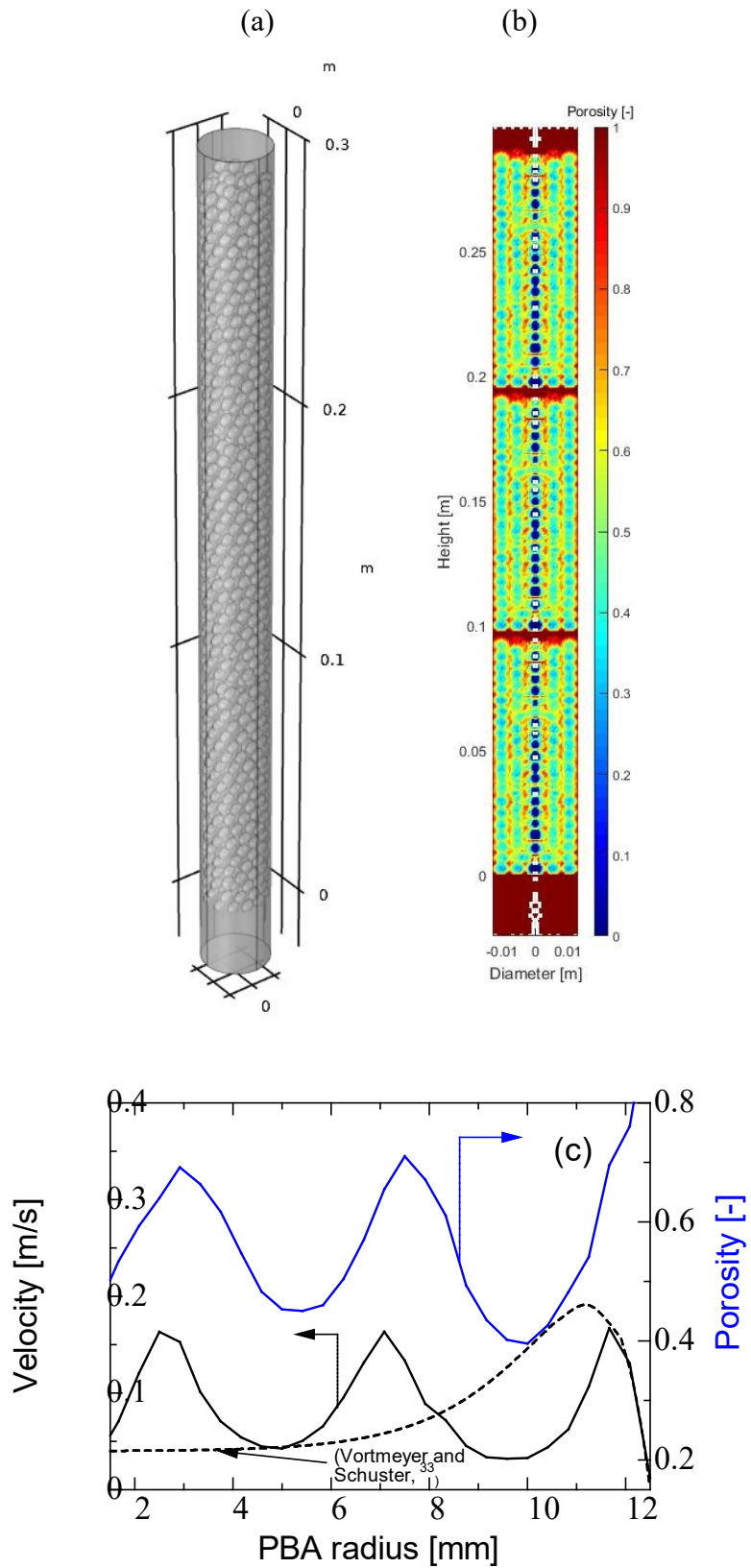


Figure 1 Structural distribution of the packing, (a) DEM built structure; (b) 2D circumferentially averaged porosity and (c) circumferentially and axially averaged porosity and velocity. PBA of 25 mm ID, 300 mm length, AR of 5 and feed inlet velocity of 0.096 m s^{-1}

1.3 Fluid Flow Model

1.3.1 Flow model

The flow inside the packed bed was described by the Navier-Stokes equations for momentum and conservation of mass (equations 4 and 5). Both pressure and viscous forces were applied to a compressible fluid under a laminar flow. The temperature-dependent physical properties (i.e., density, viscosity, thermal conductivity and thermal capacity) relevant to both the gaseous and the catalytic phases were obtained from the built-in data base of COMSOL, or literature as illustrated in **Table 1**.

$$\rho_g(u \cdot \nabla u) = -\nabla p I + \nabla \cdot \left(\mu(\nabla u + (\nabla u)^T) - \frac{2}{3} \mu(\nabla \cdot u) I \right) \quad (4)$$

$$\rho_g \nabla \cdot u = 0 \quad (5)$$

where ρ_g is the density of the gaseous phase, p is the static pressure, μ is the dynamic viscosity, u is the velocity vector and I denote the identity matrix. Atmospheric pressure at the exit, fixed velocity at the inlet, and no-slip conditions at the solid–gas contact points were assumed.

Two material balance models were implemented by defining the solid phase and gas phase separately. The gas phase material balance (equation 6) included the rates for the diffusional and convective transports while the pores of the solid phase (equation 7) included the rates of diffusional transport and adsorption.

$$\frac{\partial c_{i,g}}{\partial t} + \nabla \cdot \left(-D_{i,g} \nabla c_{i,g} \right) + u \cdot \nabla c_{i,g} = 0 \quad (6)$$

$$\frac{\partial c_{i,pore}}{\partial t} + \nabla \cdot \left(-D_{i,s} \nabla c_{i,pore} \right) = -R_{ads,i} \quad (7)$$

The model of diffusivity in the solid phase $D_{i,s}$ included the textural parameters according to models of non-structured porous networks and was estimated according to Equations 8-10 by considering both Knudsen D_i^K and bulk solid types of diffusion D_i^b .

$$\frac{1}{D_{i,s}} = \frac{1}{D_i^b} + \frac{1}{D_i^K} \quad (8)$$

$$D_i^b = \frac{\varepsilon_s D_{i,g}}{\tau_s} \quad (9)$$

$$D_i^K = \frac{2}{3} r_p \sqrt{\frac{8RT}{\pi M_i}} \frac{\varepsilon_s}{\tau_s} \quad (10)$$

The diffusivity values in the gaseous phase $D_{i,g}$ were approximated to the molecular diffusivity of these species in each other due to the low concentrations used as illustrated in **Table 1**, M_i is the molecular weight, r_p is the average pore radius of zeolite and ε_s and τ_s are the textural parameters of particles in terms of bed porosity and tortuosity, respectively^{24,25}.

The heat balance model is analogous to the material balance that includes two equations for the solid and gas phases. There is a convective heat transfer term in the gas phase and a heat generation term in the solid phase to account for heat of adsorption of CO₂ and N₂. Equations 11 and 12 describe the energy balance in the gas and solid phases, respectively.

$$\rho_g c_{p,g} \frac{\partial T}{\partial t} + \rho_g c_{p,g} u \cdot \nabla T = \nabla \cdot (k_g \nabla T) \quad (11)$$

$$\rho_s c_{p,s} \frac{\partial T}{\partial t} = \nabla \cdot (k_s \nabla T) + \Delta H_{ads} R_{ads,i} \quad (12)$$

where $c_{p,g}$ and $c_{p,s}$ are the heat capacity of the gaseous and solid adsorbent phases, respectively, k_g and k_s are the thermal conductivity of the gaseous and solid phases, respectively.

The wall of the PBA was assumed to be exposed to thermal cooling by the environment surrounding the wall of the PBA. The rate of heat loss Q is expressed by Equation 13, depending on gas-wall or particle-wall contact points²⁶.

$$h_{ext}(T - T_{ext}) = \nabla \cdot (k_w \nabla T) \quad (13)$$

Where T_{ext} is the ambient temperature outside of the packed bed, ΔH_{ads} is the enthalpy of the reversible adsorption, h_{ext} is the heat transfer coefficient through the wall-surrounding film of the PBA²⁷ and k_w are the thermal conductivity of the wall²⁸.

$$Nu = \frac{h_{ext}D}{k_g} = \left[0.6 + 0.387 \frac{Ra^{1/6}}{\left[1 + \left(\frac{0.559}{Pr} \right)^{9/16} \right]^{8/27}} \right]^2 \quad (14)$$

where D is the external wall diameter, Pr is the Prandtl number and Ra is Rayleigh number at the average temperature.

1.3.2 Adsorption Model

The 3D model discriminates between the rates of transports and the rate of adsorption. It accounts for loss of species i from the gaseous phase in the pores to the surface of the adsorbent, as expressed by equations 15 (a,b).

$$R_{ads,i} = a \frac{\partial c_{i,s}}{\partial t} \quad (15a)$$

Where c_s is the surface concentration and a is the pore surface area to volume ratio (m^2/m^3) of the sorbent.

$$a = \frac{\rho_s S}{\varepsilon_s} \quad (15b)$$

Since adsorption of both CO_2 and N_2 follow a physical type of adsorption (i.e. $\Delta H_{ads,CO_2/zeolite\ 13X}$ and $\Delta H_{ads,N_2/zeolite\ 13X}$ are 36 and 25 $kJ\ mol^{-1}$, respectively, as illustrated in **Table 1**), the kinetics of surface adsorption is considered fast to reach an equilibrium state³. By applying the chain rule to dependent variable $c_{i,pore}$, the rate of surface adsorption becomes proportional to that in the pores.

Table 1 Physical property for adsorbents on zeolites

Physical property	Simulation
$C_{p,Zeolite\ 13X}$ [$J\ kg^{-1}\ K^{-1}$] ²⁹	920
$k_{Zeolite\ 13X}$ [$W\ m^{-1}\ K^{-1}$] ³⁹	0.125
Heat Capacity of gas, c_p (J/kgK) ⁴⁰	1930
$\rho_{Zeolite\ 13X}$ [$kg\ m^{-3}$] ⁴⁰	1930
$\Delta H_{ads,CO_2/zeolite\ 13X}$ [$kJ\ mol^{-1}$] ²⁹	36
$\Delta H_{ads,N_2/zeolite\ 13X}$ [$kJ\ mol^{-1}$] ²⁹	25
a [m^2/m^3] ⁴⁰	3.95×10^6
$S_{zeolite\ 13X}$ [$m^2\ g^{-1}$] ²⁹	675
D_{CO_2-air} [$m^2\ s^{-1}$] ^{21,36}	$1.1 \times 10^{-7}T(^{\circ}C) - 1.8 \times 10^{-5}$
D_{N_2-air} [$m^2\ s^{-1}$] ^{21,36}	$1.5 \times 10^{-7}T(^{\circ}C) - 2.6 \times 10^{-5}$
ϵ_s [-] ²⁹	0.33

$$R_{ads,i} = a \frac{\partial c_{i,s}}{\partial t} = a \frac{dc_{i,pore}}{dt} \left(\frac{dc_{i,s}}{dc_{i,pore}} \right) \quad (16)$$

The term $\left(\frac{\partial c_{i,s}}{\partial c_{i,pore}} \right)$ is the slope of Langmuir isotherm model reported suitable for the weak interactions between N_2 and CO_2 at N_2 composition of less than 20 %²⁹⁻³¹. The ideal adsorption solution theory then applies to the quantity adsorbed as expressed by equation 17.

$$c_{i,s} = \frac{q_i}{S} = \frac{q_{s,i} b_i p_{i,pore}}{S(1+b_i p_{i,pore})} \quad \text{where} \quad b_i = b_{0,i} e^{b_{1,i} T} \text{ and } q_{s,i} = q_{0,i} e^{q_{1,i} T} \quad (17)$$

Where q_s is the adsorbed quantity, S is surface area per unit mass of adsorbent, and p_i is the partial pressure of component i . Adsorption constants q_0 , q_1 , b_0 and b_1 for CO_2 and N_2 adsorption on zeolite 13 X are illustrated in **Table 2**.

After differentiation of Equation 17 with respect to $c_{i,pore}$ and substitution in Equation 16.

$$R_{ads,i} = a \frac{\partial c_{i,s}}{\partial t} = a \frac{\partial c_{i,pore}}{\partial t} \frac{q_{s,i} b_i RT}{S(1+b_i c_{i,pore} RT)^2}, j \neq i, k = 1,2 \quad (18)$$

Which then leads the models of mass and heat balance in the pores (equations 7 and 12) to become function of concentration of species in the pore phase only, as expressed by equations 19 and 22, respectively.

$$\left(a \frac{q_{s,i} b_i RT}{S(1+b_i c_{i,pore} RT)^2} + 1 \right) \frac{\partial c_{i,pore}}{\partial t} + \nabla \cdot (-D_{i,s} \nabla c_{i,pore}) = 0 \quad (19)$$

$$\rho_s c_{p,s} \frac{\partial T}{\partial t} = \nabla \cdot (k_s \nabla T) + \Delta H_{ads} a \frac{\partial c_{i,pore}}{\partial t} \left(\frac{q_{s,i} b_i RT}{S(1+b_i c_{i,pore} RT)^2} \right) \quad (20)$$

$$\frac{\partial c_{i,pore}}{\partial t} = \frac{D_{i,s}}{\left(a \frac{q_{s,i} b_i RT}{S(1+b_i c_{i,pore} RT)^2} + 1 \right)} \nabla^2 c_{i,pore} \quad (21)$$

$$\frac{\partial T}{\partial t} = \frac{k_s}{\rho_s c_{p,s}} \nabla^2 T + \frac{\Delta H_{ads}}{\rho_s c_{p,s}} \left(a \frac{q_{s,i} b_i RT}{S(1+b_i c_{i,pore} RT)^2} \right) \frac{\partial c_{i,pore}}{\partial t} \quad (22)$$

Where $\frac{D_{i,s}}{\left(a \frac{q_{s,i} b_i RT}{S(1+b_i c_{i,pore} RT)^2} + 1 \right)}$ and $\left(a \frac{q_{s,i} b_i RT}{S(1+b_i c_{i,pore} RT)^2} + 1 \right)$ are the effective diffusion and packing

Henry law constants, respectively. Before simulations could be initiated, the boundary conditions were set (i.e., an initial concentration of 0.001% of CO₂ concentration in the carrier gas N₂, atmospheric pressure at the exit, uniform velocity and temperature across the inlet plane and no slip condition at all solid boundaries (i.e., particle and wall)). The fluid flow equations were first solved in a steady state condition prior to solving the time dependent equations, allowing action as an initial boundary condition for the dynamic terms (mass, heat and adsorption). The integration of the governing equations was carried out by discretisation into finite elements by using sets of difference equations. The generalized minimal residual method with the Geometric Multigrid preconditioner algorithm was used to approximate the solution at minimum residual values. The built-in meshing module of COMSOL, which includes an adaptative mesh refinement procedure, allowed investigation of effect of the size of the elements on the fluid flow model and validation by a mesh convergence test. The pressure values at three locations were assessed by using the Grid Convergence Index (GCI). Errors due the discretisation procedure were assessed by following the procedure recommended by Celik et al.³², validating that the results were not affected by mesh size. A solution, irrespective of mesh size, was reached when the GCI was below 3.1%. The simulation was carried out using COMSOL Multiphysics 5.3 and a single 512 GB RAM computer server by Dell incorporation which was equipped with Intel Xeon E5-2637 v3 specification and 4 cores 3.50 GHz.

Table 2 Adsorption isotherm parameters for the Langmuir isotherm model ²⁹

Constants*	Zeolite 13X	
	CO ₂	N ₂
q _{0,i} [mol kg ⁻¹ Pa ⁻¹]	2.38341	0.06355
q _{1,i} [K ⁻¹]	-0.02816	-0.02934
b _{0,i} [Pa ⁻¹]	0.12266	6.313x10 ⁻⁴
b _{1,i} [K ⁻¹]	-0.02353	-0.01419

$$*q_i = \frac{q_{s,i} b_i p_i}{1 + \sum_k b_{i,k} p_{i,k}} = \frac{q_{0,i} e^{q_{1,i} T} b_{0,i} e^{b_{1,i} T} p_i}{1 + \sum_k b_{0,i,k} e^{b_{1,i,k} T} p_{i,k}}$$

$$c_{i,s} = \frac{q_i}{S} = \frac{q_{s,i} b_i p_{i,pore}}{S(1 + b_i p_{i,pore})} \quad \text{where} \quad b_i = b_{0,i} e^{b_{1,i} T} \text{ and } q_{s,i} = q_{0,i} e^{q_{1,i} T} \quad (17)$$

2. Results and discussions

2.1 Velocity profiles inside the packed bed

The structure of the packing impacted the way in which the flow of CO₂ passed through the void regions of the packing, driving variation in velocity, and thus convective transfers of mass and heat, depending on the local topology. Since a low AR packing (i.e., AR 5) was used, it introduced effect of the wall on the structure of the packing as reported in section 2.2 and additional impact on adsorption caused by the channelling at the outer regions of the bed²¹.

Figure 1 (c) and **Figures 2 (a) and (b)** show profiles of circumferentially and axially averaged velocity, circumferentially averaged velocity and cross-axial velocity, respectively, along the PBA when it was operated at an inlet velocity of 0.096 m s⁻¹ ²⁹. The results were compared with the model of Vortmeyer et al.³³ who solved the modified Brinkman equation for fluid flow and accounted for the walls presence. It is observed an increase in velocity near the wall due to the preferential channelling effect before it subsided due to the no slip at the solid boundaries. Local circumferentially averaged velocities in **Figure 2 (a)** are seen non-uniform and function of the local bed porosity and structure of the packing. Local peaks of interstitial velocity, as observed in the axial section of the bed in **Figure 2 (b)**, have reached values of

about seven times higher than the average velocity in certain zones where more efficient mixing (**Figure 2(b)**), and by inference mass and heat transports, are anticipated.

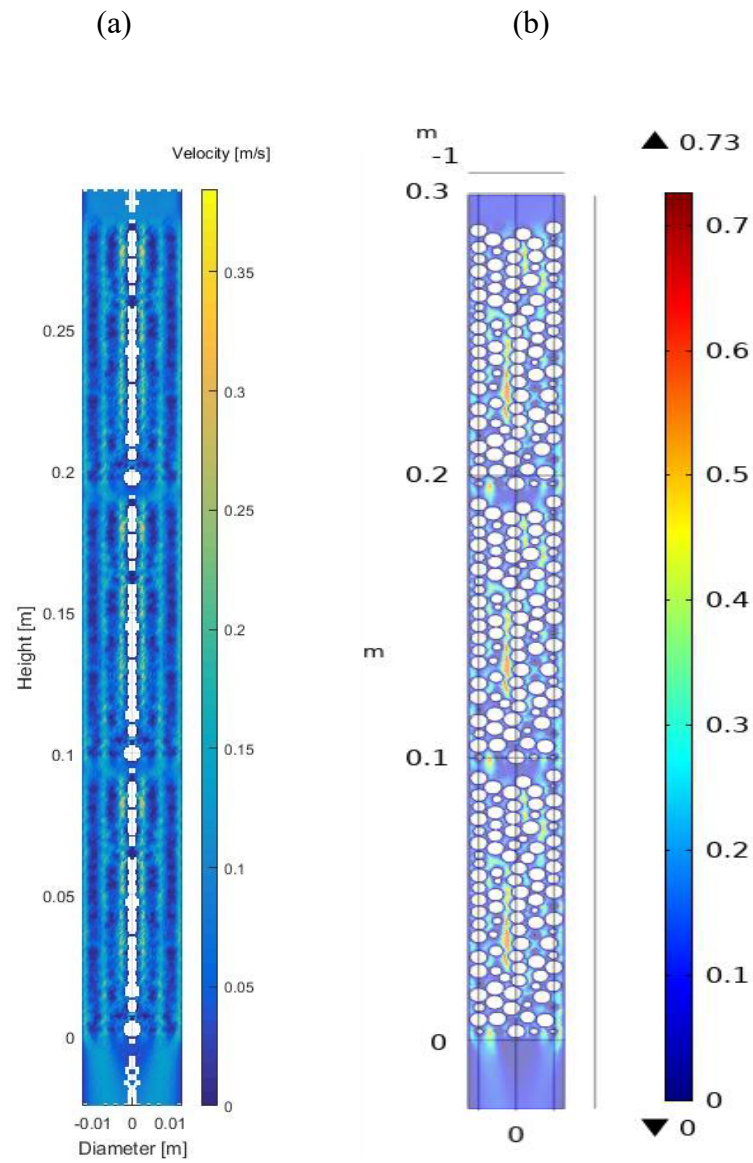


Figure 2 Interstitial velocity map (a) Circumferentially averaged (b) Axial section of the PBA.
PBA of 25 mm ID, 300 mm length, AR of 5 and feed inlet velocity of 0.096 m s^{-1}

2.2 Analysis of adsorption inside the packed bed

The effect of thermal exchange with the surrounding was studied to explore how breakthrough was affected by operations at adiabatic and non-adiabatic conditions, again by gaining access to the inside of the bed.

In case of dual adsorption case, the governing equations were set up in the same manner for both CO₂ and nitrogen gases and inlet feed CO₂ mole fraction gas in N₂ was set to 15%. **Figure 3** shows the isotherms of CO₂ and N₂ on zeolite 13X at 20°C and 15% CO₂ mole fraction, where the capacity for CO₂ was far greater than for N₂²⁹. The adsorption isotherm of the binary mixture followed the ideal adsorbed solution theory model and nitrogen was hardly adsorbed when its mole fraction was less than 0.8 but importantly did not affect the equilibrium amount of CO₂, validating application of ideal adsorption solution theory. The isosteric heat of adsorption for CO₂ and N₂ were set to 36 kJ and 25 kJ, respectively, which indicates a stronger affinity to CO₂³⁴. It can be seen in **Figure 4 (a)** with the N₂ component, the breakthrough occurred as soon as the transient process began. There were two processes driving this early breakthrough; firstly, the adsorption process was not able to sufficiently store N₂ on the solid surface because of slow kinetics (low gradient) and low capacity (small plateau). Secondly, the competition existed between the CO₂ and N₂, and because CO₂ had higher kinetics and capacity, it saw higher selectivity for storage on the solid surface. This is supported by the fact that a higher energy was released for CO₂ adsorption. The exit temperature for the dual adsorption is shown in **Figure 4 (b)** where the first the breakthrough peak of temperature was for N₂ but with lower values of heat of adsorption and adsorption capacity.

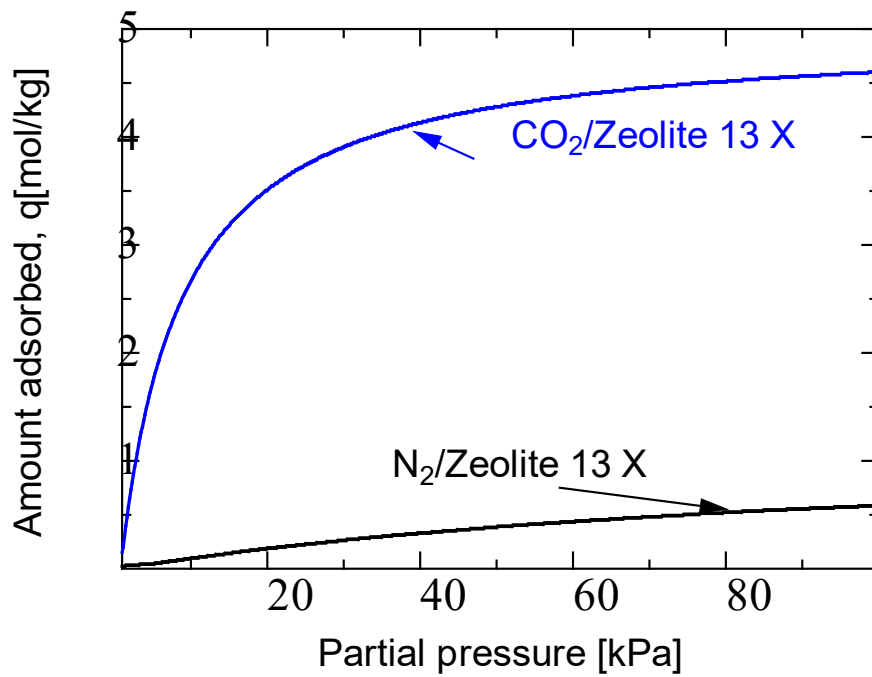
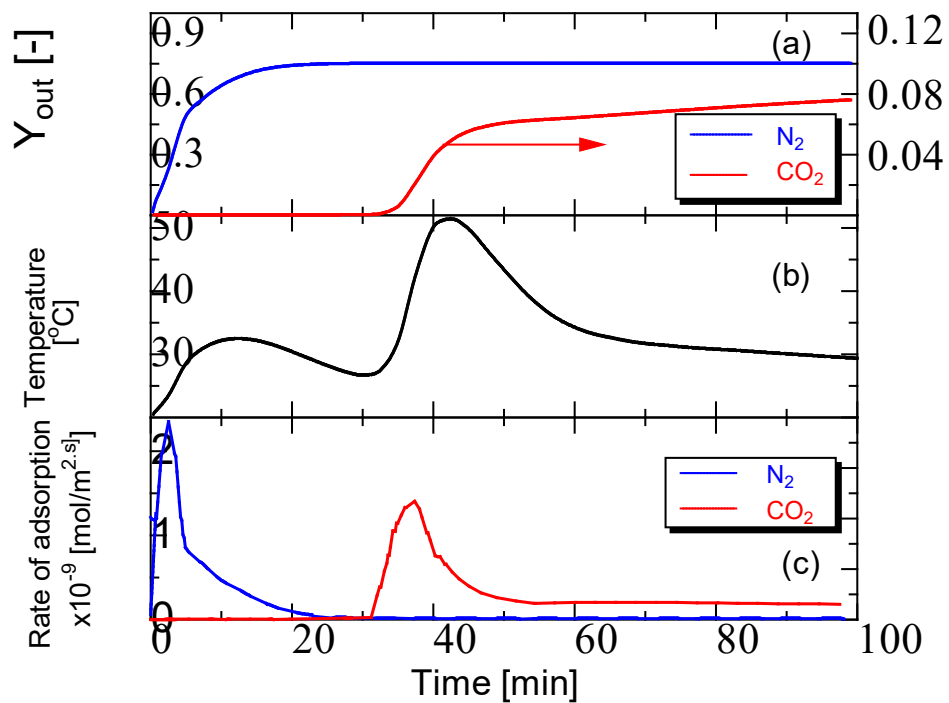


Figure 3 Adsorption isotherms of CO₂ and N₂/zeolite 13X at 20 °C.²⁹



Figures 4 Breakthrough mole fraction (Y_{out}) (a) temperature (b) and adsorption rate (c) profiles for the dual adsorption of CO₂ and N₂. PBA of 25 mm ID, 300 mm length, diffusivity of 10^{-8} m²/s, AR of 5, feed inlet velocity of 0.096 m, inlet temperature of 20°C and h_w of 9.5 W/m²K

The average rate of adsorption occurring in the particles located at the exit of the packed bed could be taken over the transient interval for both N₂ and CO₂, along with the average temperature, as seen in **Figure 4 (c)**. The first temperature peak was accompanied by an increased peak rate of N₂ adsorption, and the second a large peak rate of CO₂ adsorption. The rate of the peaks, denoted by $\frac{\partial c_{i,s}}{\partial t}$, validates the relationship between temperature of adsorption and the rate of mass transfer in the solid phase. The rate peak of N₂ was higher than that of CO₂ while the amount of N₂ transferred to the solid phase was significantly lower, and so the overall heat released was less. As well as this, the mole fraction of N₂ in the gas phase was much higher than that of CO₂, and so the initial driving force was large. It is observed then when large breakthrough waves (larger mass transfer zones) were present, the leading concentration was lower, which made the rate also lower, as seen in the comparison of solid diffusivity (where lower diffusivities led greater temperature peaks).

Figure 5 shows axial sections of mole fraction profile inside the adsorber after 25 minutes of operation. By this point, the N₂ had already broken through, and its uptake had virtually ceased. What is noticeable is the particle saturation level of both solutes. For N₂, the solid phase was almost completely saturated, with a penetration reaching the centre of the particle. For CO₂, the saturation had only occurred near the edge. This suggests that the uptake was still ongoing in the central regions of the particles and that CO₂ was still being transferred to the adsorbed phase. This ongoing adsorption is supported by presence of the breakthrough tailing.

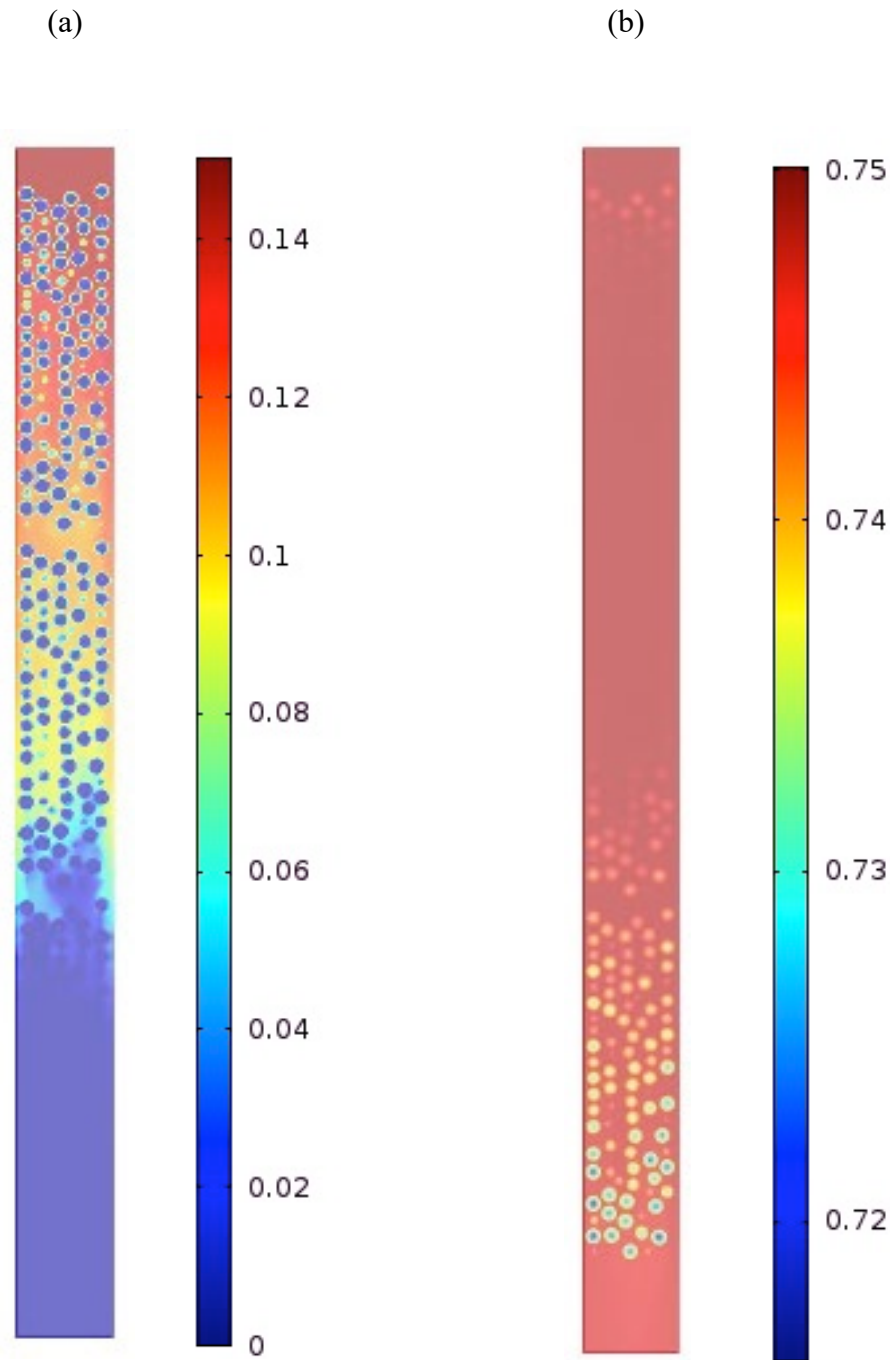


Figure 5 Axial section of mole fraction of CO₂ (a) and N₂ (b) after 25 min, inlet mole fraction of CO₂ $Y_{CO_2}=0.15$ and $Y_{N_2}= 0.75$. PBA of 25 mm ID, 300 mm length, diffusivity of 10^{-8} m²/s, AR of 5, feed inlet velocity of 0.096 m, inlet temperature= $20^{\circ}C$ and h_w of 9.5 W/m²K

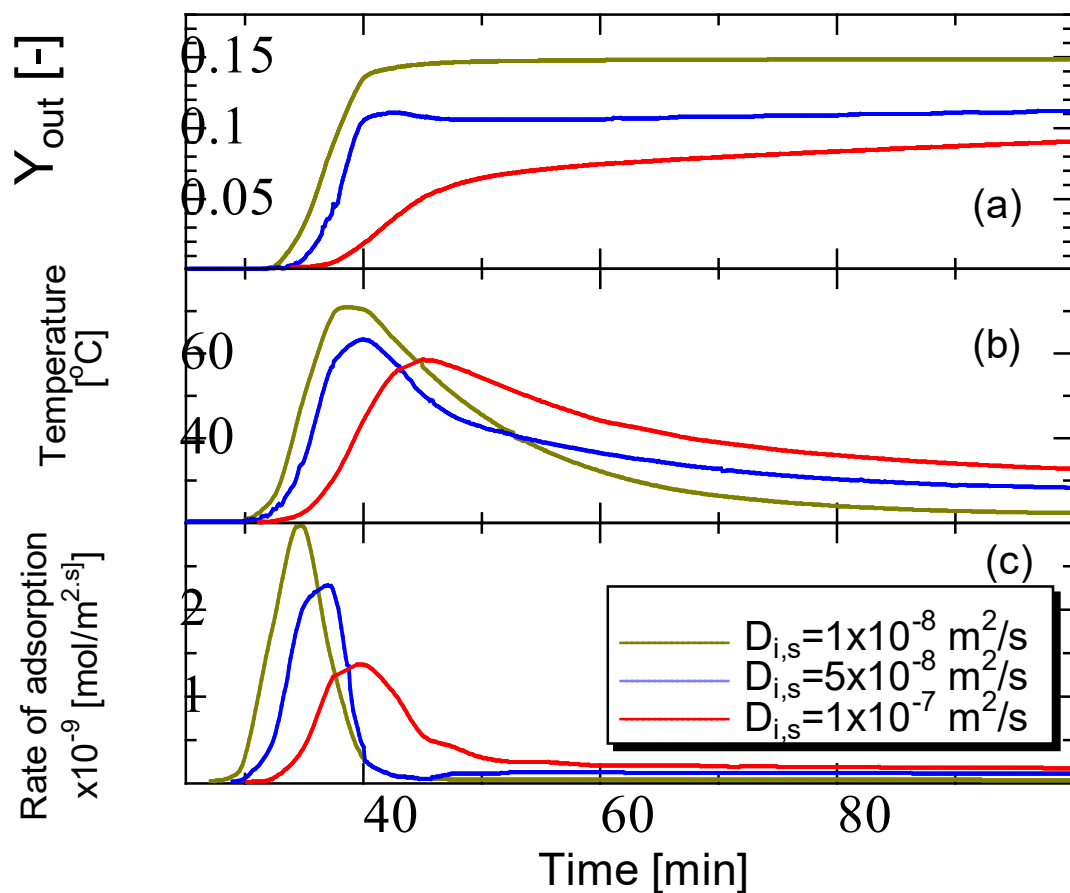
2.2.1 Effects of internal mass transfer on adsorption profiles

The diffusivity of CO₂ inside porous solids is a function of the pore network at various scales (i.e., micro- to macro-pores) within zeolite and presence of N₂³⁵. It is therefore important to

gain a perspective into effect of the diffusion magnitude, as this represents different materials and can vary by orders of magnitude for a single material. According to equations 6-8, the diffusion of CO₂ inside zeolite 13X may vary between 10⁻⁶ (macroporous) and 10⁻⁸ (microporous) m²/s, depending on the structure of the pores³⁶. This variation in porosity has been investigated by surface coating (i.e. tuning the hydrophilic property for the reduction of water vapour inhibition, chemical impregnation and ion-exchange for the promotion of CO₂ intake⁷⁻⁹).

Figure 6 (a-c) show the breakthrough in terms of mole fraction, temperature, and adsorption rates profiles at the exit for diffusivity values ranging from 10⁻⁸ to 10⁻⁷ to m²/s (i.e., r_p from 2 to 5 to nm). The curves in **Figure 6 (a)** show a steep initial shape before levelling off. The onset of concentration breakthrough occurred earlier for the case of low diffusivity due reduced mobility of CO₂ and breakthrough. The gradient of the concentration breakthrough curve was a function of the mass transfer zone (MTZ) that is undergoing dynamic adsorption and reflected by an observable wave moving through the bed. Wide MTZs associated with a pronounced tailing in the breakthrough curves were present for large diffusivity (i.e. $D_{i,s}$ of 1x10⁻⁷ m²/s). The tail shows a gradual increase in outlet concentration, while for reduced diffusion rate, the plateau front progressed towards a flat shape. When the diffusivity was set low however, undesirable features such as little forewarning that the onset of breakthrough was beginning and resulted in high concentrations of CO₂ at the outlet. The wide MTZ and breakthrough tail occurred as a result of the prolonged adsorption kinetics driven by CO₂ diffusion further into the solid particles. Large MTZs and breakthrough curve tailings are undesirable for process operations as they lead to low utilisation of the solid where the shallow curve is. For the case of higher diffusivity, a double breakthrough event occurred. The double breakthrough event is the result of the breakthrough wave interference of heat and mass when they travel along the packed bed and lead to either overshoot or undershoot values in amplitudes

of the concentration and temperature along the bed length. The first was associated with an initial steeper increase in concentration at the outlet, and the second was associated with a shallower tailing of the curve, and later associated with the catching up of the breakthrough wave as a complete breakthrough occurred. The catchup behaviour at high diffusivities was more pronounced as the uptake was prolonged by the steeper loading at the wall due to channelling. This behaviour led to elevated temperature and reduced uptake which was followed by a reduced temperature due to the convective cooling and heat losses to the surrounding, once the first breakthrough has occurred.



Figures 6 Breakthrough mole fraction (Y_{out}) (a), temperature (b) and adsorption rates (c) profiles for CO_2 adsorption on zeolite 13X. Diffusivity values ranging from 1×10^{-7} to $1 \times 10^{-8} \text{ m}^2/\text{s}$, 300 mm length, AR of 5, feed inlet velocity of 0.096 m, PBA of 25 mm ID, 300 mm length, AR of 5, feed inlet velocity of 0.096 m, inlet mole fraction of 0.15, inlet temperature of 20°C and h_w of $9.5 \text{ W}/\text{m}^2\text{K}$

Figure 7 shows axial profiles of CO₂ inside the gas and solid phases of PBA over the 1D representation. The breakthrough wave was initially curved and became more linear as time goes on. There are no discontinuities in the lines covering both phases, underlying low resistance to mass transfer in area surrounding the solid particles. The peaks of concentration drops in the pores of the particles are visible along the bed length but particularly at the front end. The 1D representation does not offer sufficient details on the phenomena that are taking place in the PBA and therefore the 2D maps in **Figure 8** provides wider representations of the breakthrough dynamics, including along the radial distribution at three value of diffusivities (i.e. $D_{i,s} = 10^{-7}$, 5×10^{-8} and 10^{-8} m²/s). The point just before the exit breakthrough begins (for $t=35$ min), the point at which breakthrough is occurring (for $t=40$ min) and the point at which the plateau is reached for $t= 45$ min). There is a noticeable width of the mass transfer zone for the highest diffusivity value ($D_{i,s} = 10^{-8}$ m²/s), which covers well over two thirds of the bed length at 35 minutes. For $D_{i,s} = 1 \times 10^{-8}$ m²/s, there is a narrow mass transfer zone, that results the steep breakthrough curve seen in figure 6. Wide mass transfer zones cause pronounced tailing in the breakthrough curves that are especially present in the case of $D=1 \times 10^{-7}$ m²/s. The tail shows a gradual increase in outlet concentration, while for reduced diffusion rate, the plateau front is very flat. In an application sense, larger mass transfer zones and breakthrough curve tailing are undesirable for process operation, since there is lower utilisation of the solid and a wide range of low utility where the shallow curve is.

For steep breakthroughs, as illustrated by axial mole fraction maps of CO₂ at various values of diffusivity and adsorption time in **Figure 8**, a narrow MTZ existed and when the gradient was shallower, a wider MTZ was developed. **Figures 8 (a1,b1,c1)**, **Figures 8 (a2,b2,c2)** and **Figures 8 (a3,b3)** illustrate mole fraction maps at the point just before breakthrough began, the point at which breakthrough was occurring and the point at which the plateau was reached. It is apparent that for highest diffusivity, there was a noticeable development of the width of the

MTZ, which covered well over two thirds of the bed length at 35 minutes. For $D=1 \times 10^{-8} \text{ m}^2/\text{s}$, there was a narrow width of the MTZ, that resulted in the steep breakthrough curve seen in

Figure 8.

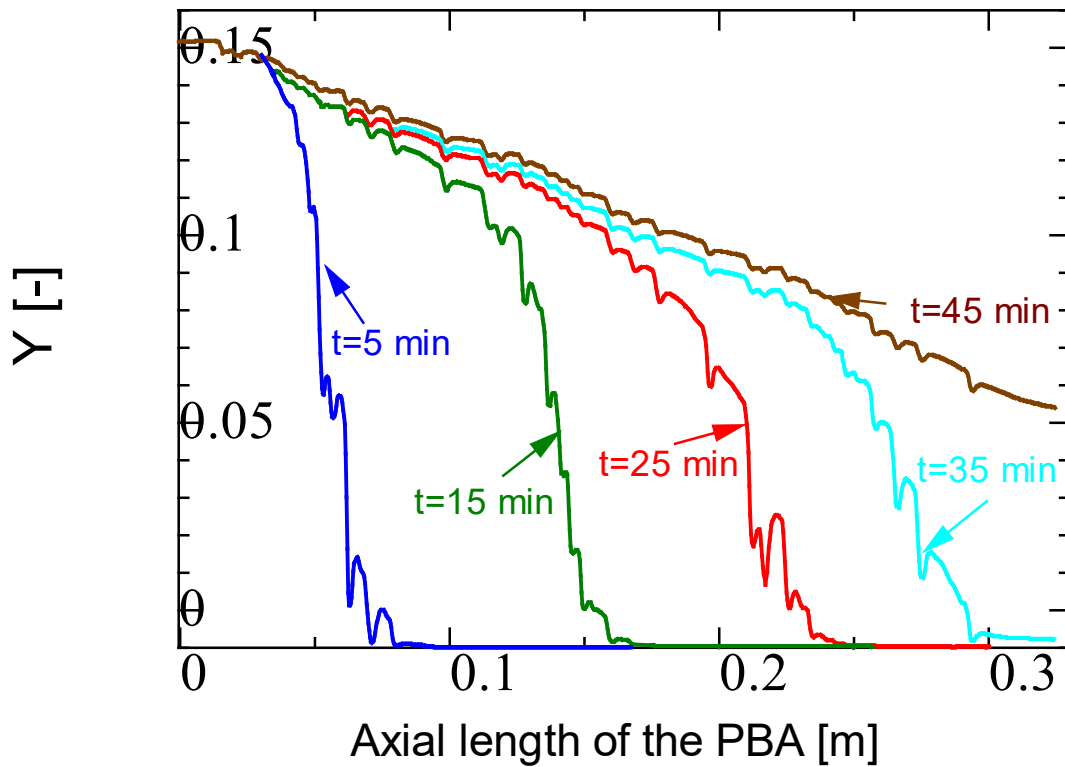


Figure 7 Transient profiles of axial mole fraction Y [-] along the PBA. PBA of 25 mm ID, 300 mm length, AR of 5, feed inlet velocity of 0.096 m and diffusivity of CO_2 of $1 \times 10^{-7} \text{ m}^2/\text{s}$, PBA of 25 mm ID, 300 mm length, AR of 5; feed inlet velocity of 0.096 m, inlet mole fraction of CO_2 of 0.15, inlet temperature of 20°C and h_w of $9.5 \text{ W}/\text{m}^2\text{K}$.

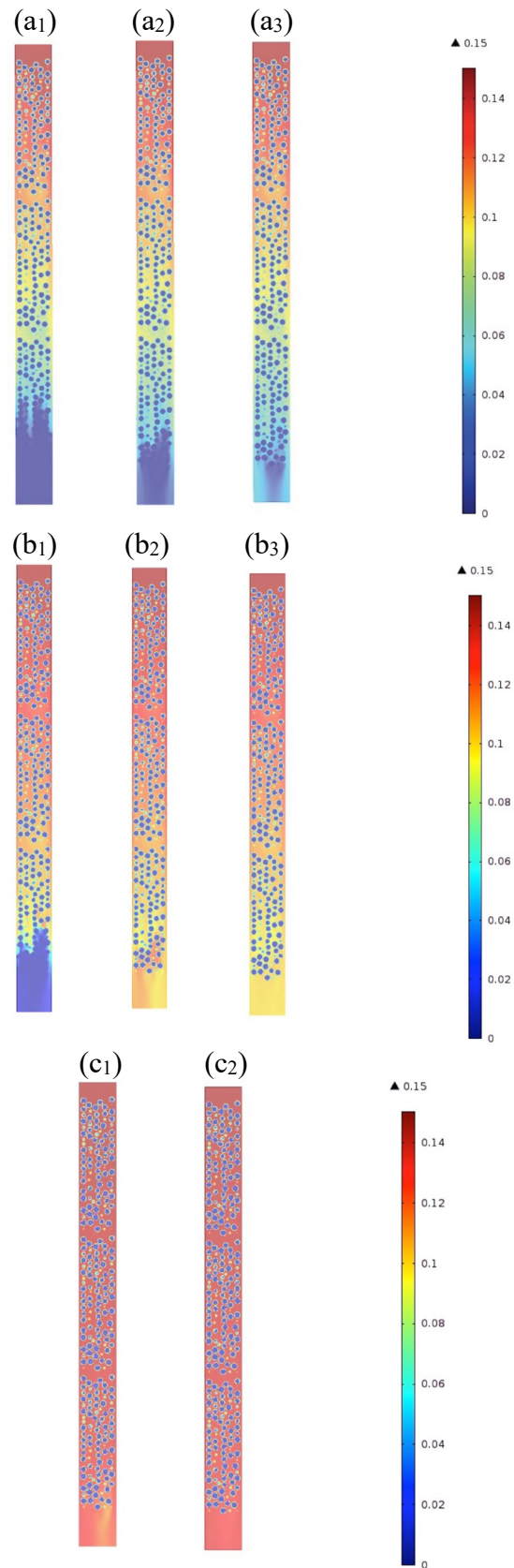


Figure 8 Axial sections of mole fraction (Y) of CO_2 along the PBA. (a), (b) and (c) for $D_{i,s} = 10^{-7}$, 5×10^{-8} and $10^{-8} \text{ m}^2/\text{s}$, respectively, and subscripts 1, 2 and 3 for $t = 35, 40$ and 45 min , respectively, PBA of 25 mm ID, 300 mm length, AR of 5, feed inlet velocity of 0.096 m, inlet mole fraction of CO_2 of 0.15, inlet temperature of 20°C and h_w of $9.5 \text{ W/m}^2\text{K}$

Interestingly, these figures show that the bulk cross-section of gaseous phase was more saturated with CO₂. It should be noted that, unlike the mass transfer resistance, the heat transfer resistance inside the particles was negligible (i.e., low values of Biot and Stanton numbers) due to reduced gradients of temperature inside the particles. The trends of this saturation followed the velocity map cross-section and thus demonstrated the non-relevance of external mass transfer around the particles. Inside the particles however, gradients of concentrations are observed and by inference the relevance of the inner mass transfer resistance. The range of inner saturation varied from fully depleted area at the centre of particles to progressive depletion at the periphery of the particles. At inter-particle scale, the concentrations of CO₂ are higher at the centre of the PBA than the periphery regions and these concentrations followed well the trends of concentrations in the bulk gaseous phase. These gradients inside the particles increased as the particles were filled up with CO₂. Overall, at low diffusivity, the profiles of mole fraction maps inside the particles were symmetric and thus were less affected by the surrounding bulk phase. The diffusion rate was the same, despite the uneven mass transfer rate around the particles. At high values of diffusivity, the concentration inside the particle was however affected by the particle surroundings observed by the angular asymmetry.

2.2.1.1 Temperature profiles

The mole fraction breakthrough curves for the three diffusion rates were accompanied by the non-isothermal temperature curves as shown in **Figure 6 (b)**. These are complementary but validate once more that the onset of breakthrough occurred later in the case of increased diffusivity as mapped by the raised peaks of temperature.

The profiles of temperature show adsorption zones which is located between the onset temperature and the maximum temperature. At the front of the adsorption zone, temperature increased to the highest values whereas the downstream zones exhibited high temperature

waves before decreasing due to cooling by the flow dispersion and the wall thermal exchange. For lower diffusion rates as shown in **Figure 6 (c)**, the peaks of temperature were higher, driven by a high rate of adsorption and caused by the much smaller adsorption front for the moving breakthrough wave. For higher diffusivity, the adsorption occurred for a wider range of the bed, and since the concentration was lower at the front of the wave, the rate was also slower. Furthermore, the decay of peak of temperature at high diffusivity was slower, again due to the prolonged adsorption in place that continued to generate heat, compared to diffusion where adsorption subsided after breakthrough and inlet temperature was reached faster. The peaks of temperature were also narrower for slower diffusion and were a function of the width of the breakthrough front. Since increased access to the particles was available, more material was adsorbed, and the heat generated lasted for a longer period.

Axial sections of CO₂ mole fraction inside the PBA for each diffusion rate and after 100 minutes are shown in **Figures 9(a₁-a₃)**. For $D=1 \times 10^{-7}$ m²/s, there was an increased depth of penetration, which backs up the previous statement that greater utilisation of the solid phase has been achieved. Particle utilisation was however not high, since after a 100-minute period, the central regions in the particles are far from being saturated with CO₂, which is weakly visible near the centre of the particles. The isotherm of CO₂ onto zeolite 13X in Figure 3 is steep, which resulted in faster adsorption kinetics, leading the core regions of the particles to be devoid of CO₂ while it was still being captured from gaseous phase of the pores. Once the outer regions of the particle were saturated in CO₂, the capacity in adsorption of CO₂ by zeolites would be and so the pore gas mole fraction began to increase.

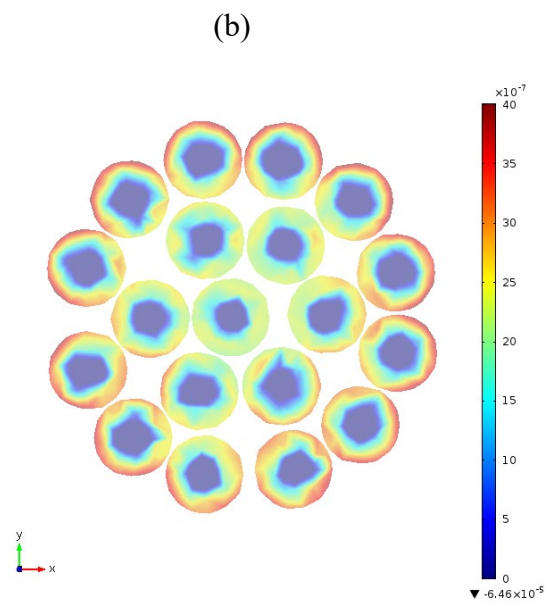
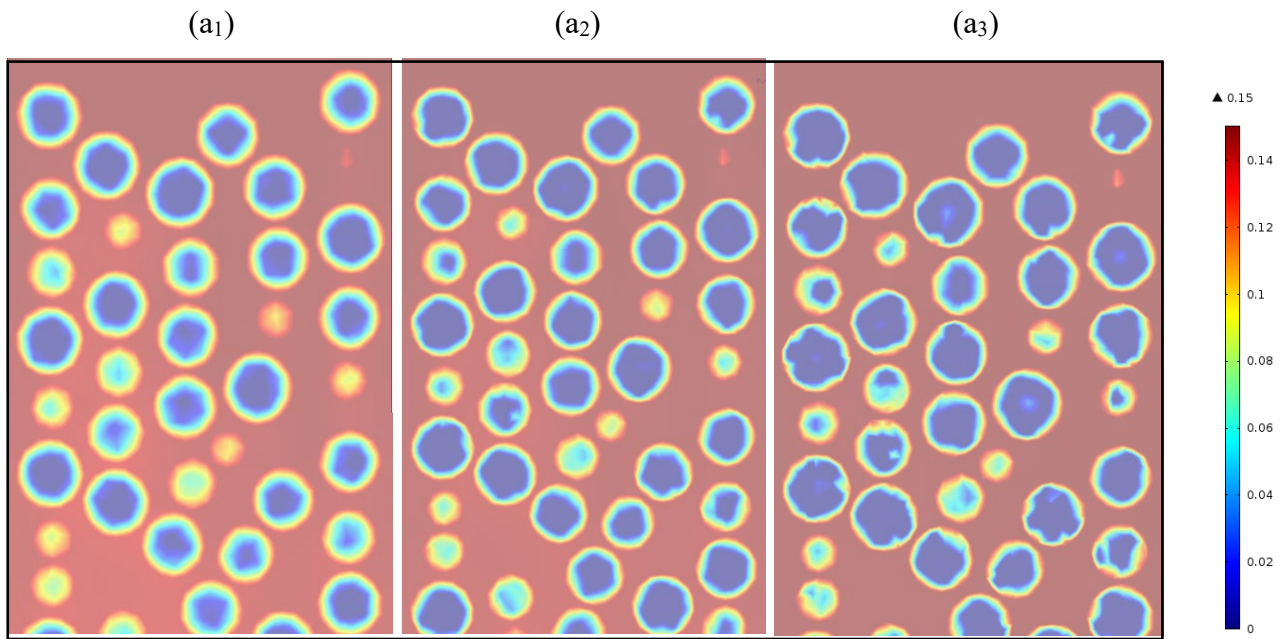


Figure 9 Axial section maps of CO₂ mole fraction (Y) for (a₁) $D_{i,s} = 1 \times 10^{-7}$, (a₂) 5×10^{-8} and (a₃) $10^{-8} \text{ m}^2 \text{ s}^{-1}$, and cross-sectional mole fraction map of CO₂ (b), time of 100 min, PBA of 25 mm ID, 300 mm length, AR of 5, feed inlet velocity of 0.096 m and inlet mole fraction of CO₂ of 0.15, inlet temperature of 20⁰C and h_w of 9.5 W/m²K

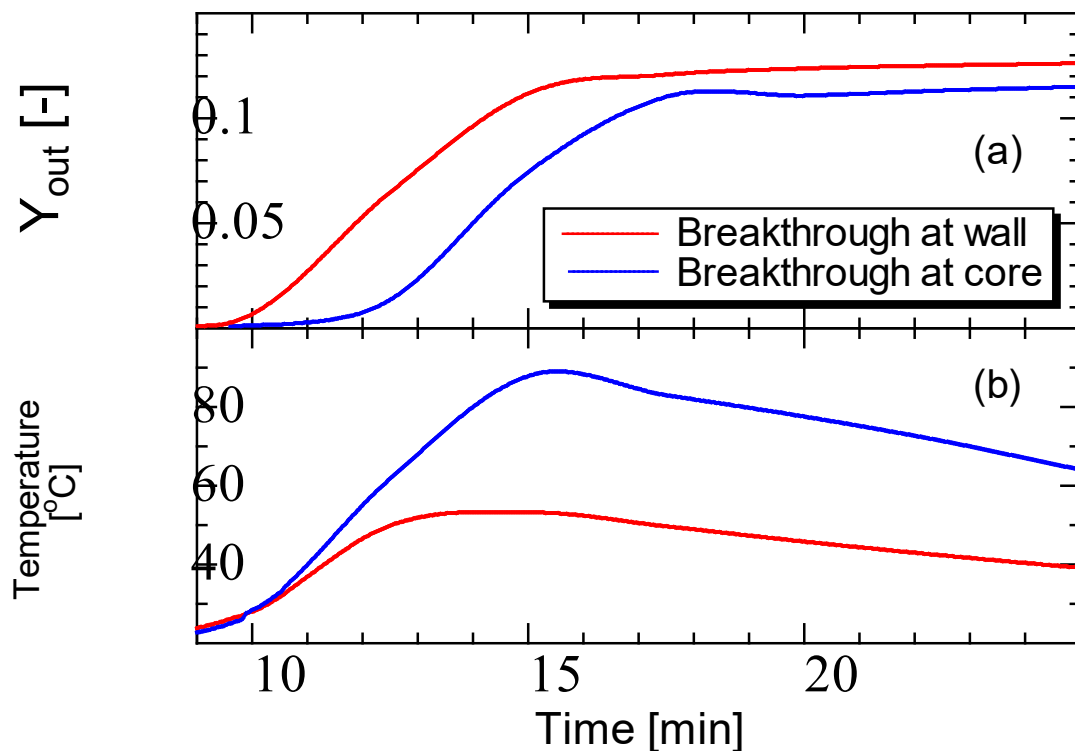
2.2.1.2 Angular non-symmetric distribution of mole fraction and temperature

When 1D and 2D pseudo homogeneous modelling methods are used, there are limited means of seeing the process occurring at local scale during its operation. In this case, adsorption uptake has been shown to vary depending on the interstitial flow and structure inside the bed. The adsorption process occurring inside the packed bed did not show entire homogeneity. **Figure 9 (b)** shows that adsorption occurred earlier at the wall region of the column, which stemmed from the structure of the packing discussed in **section 2.1** (i.e., an increased bed porosity near the wall). The result of non-uniformity of the structure is shown by increased concentrations and in agreement with the known literature on the channelling phenomena in vicinity of the wall of low AR beds^{11,37}, driven by motion of fluid into the outer porous regions due to larger flow areas. Overall, the lack of angular symmetry inside the particles is attributable to reduction in resistance to mass transfer in area of solid particles exposed to high velocities, and so, there were greater convective transports from bulk of the gaseous phase to the pores– as illustrated by the lower temperature trends near the wall.

2.2.2 Non-uniform radial distribution of CO₂ mole fraction and temperature

The breakthrough trends were later observed by taking transient data of mole fraction and temperature over the adsorption period at single points inside the bed. **Figures 10 (a, b)** show both the mole fraction and temperature breakthroughs respectively, for diffusivity of 10^{-7} m²/s at the wall and core of the PBA. The points were taken at a point midway through the column in the void space between particles. The wall region displayed an earlier onset of breakthrough because there was a reduced amount of adsorbent than in the more central regions. As well as this, the plateau concentration of the wall breakthrough was larger than in the core for the same reason.

The relevant temperature curves in **Figure 10 (b)** show analogies to those of mole fraction. Higher temperatures are observed in core of the bed because there was a reduced ability to convey heat away from the point of generation, despite the adsorption rate being greater in the wall region. At the wall, the gas flow rate was higher and so the heat has been rapidly dispersed by convection or exchanged through the wall. **Figures 11 (a, b)** show axial sections along the bed of mole fraction of CO₂ and temperature at the breakthrough front and relevant dynamic adsorption for the entire breakthrough time are illustrated in movie files, mov 1 and mov2, respectively, in the supporting information. Once more, higher mole fractions and earlier breakthrough can be seen at the wall. Temperature in core of the bed was the highest and then diminished towards the wall.



Figures 10 Breakthrough mole fraction (Y_{out}) (a) and temperature (b) profiles for CO₂ adsorption on zeolite 13X at core and wall regions of the PBA. PBA of 25 mm ID, 300 mm length, $D_{i,s}=1 \times 10^{-7}$ m²/s, AR of 5, feed inlet velocity of 0.096 m, inlet mole fraction of CO₂ of 0.15, inlet temperature of 20°C and h_w of 9.5 W/m²K.

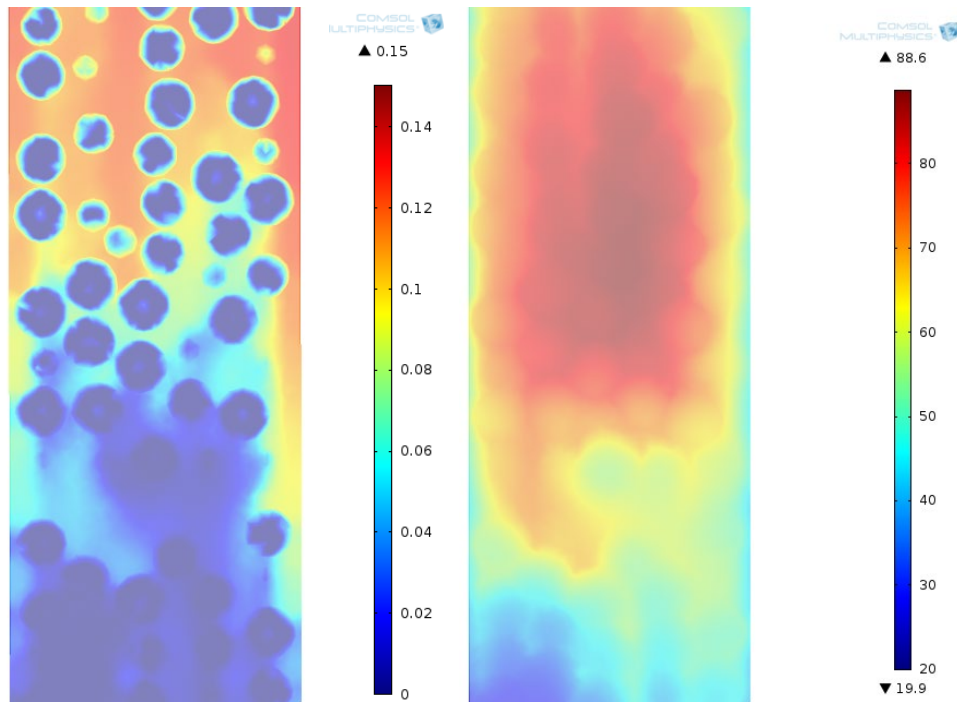


Figure 11 Axial sections of (a) mole fraction and (b) temperature for CO₂ adsorption on zeolite 13X. PBA of 25 mm ID, 300 mm length, $D_{i,s}=1 \times 10^{-7} \text{ m}^2/\text{s}$, AR of 5, time of 25 min, feed inlet velocity of 0.096 m, inlet mole fraction of CO₂ of 0.15, inlet temperature of 20⁰C, and h_w of 9.5 W/m²K

2.2.3 Catch up behaviour

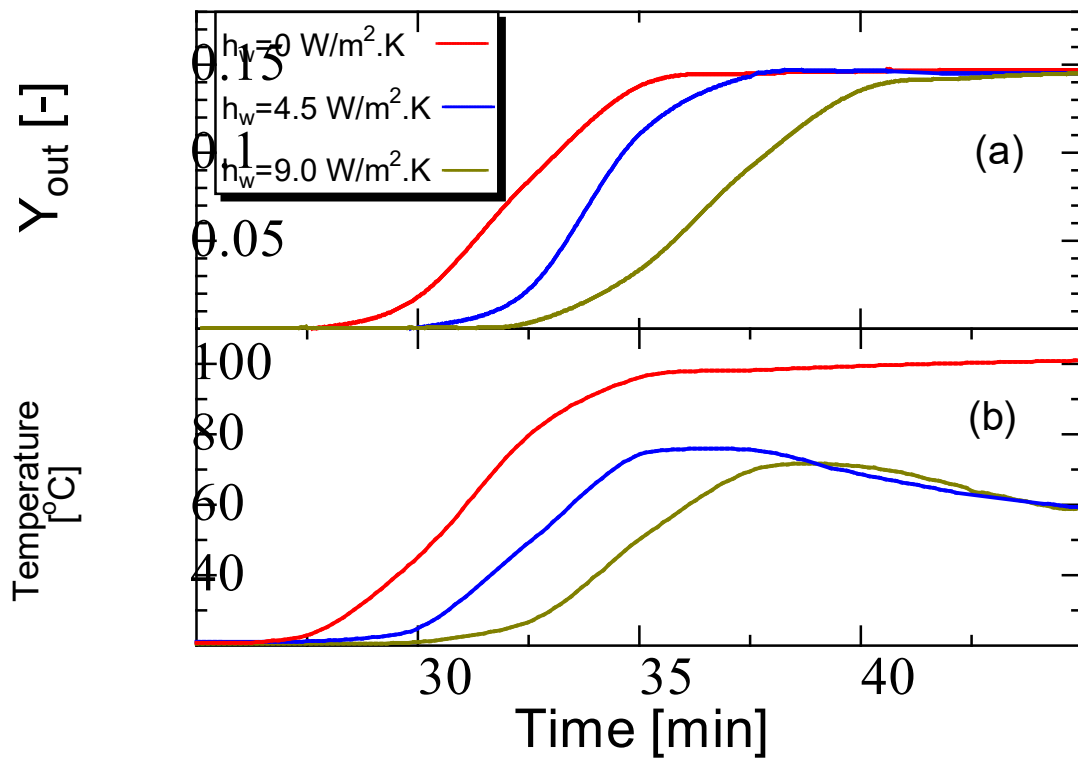
The concentration near the wall of the bed has been shown to experience breakthrough faster than in the core due to the channelling effect and increased loading at the wall. As well as this, there was another occurrence taking place. In the core, temperature was elevated to those at the wall, and so the equilibrium capacity was reduced, and less uptake occurred on the solid surface. Once the breakthrough has occurred, temperature began to decline as the heat was lost through the wall and the convective flow through the PBA. This then means that the equilibrium capacity of the core bed increased, and more adsorptions could take place, hence the outlet mole fraction decreased slightly as more material has started to transfer to the solid phase. This effect was much more profound in the core and was far more visible than at the wall (see **Figure 10 (a)**). Salem et al.³⁸ discussed similar trends in the 2D modelling of adsorption of water vapour, noting a similar lag in the core as adsorption uptake increased following a decline in temperature.

2.2.4 Effect of thermal exchange with the surrounding on the breakthrough profiles

The impact of rate of thermal exchange between the PBA and the surrounding on the breakthrough behaviour was investigated by varying the wall-surrounding heat transfer coefficient h_w , as a flexible characteristic (i.e., subject to size, geometry and position of the PBA, and to flow in the surrounding^{21,29}). The transient adsorption process was operated with values of column wall heat transfer coefficients of 9.5, 4.5 and 0 W/m²K, which correspond to a typical range of thermal exchange with ambient surrounding²⁶ and included the full thermal insulation of the PBA. **Figures 12 (a) and (b)** show the mole fraction breakthrough and corresponding temperature at the exit of the PBA for each heat transfer coefficient. Firstly, it is notable that breakthrough began at an earlier stage for the adiabatic case and occurred later as heat transfer coefficient was increased. For higher temperature, the decrease in adsorption equilibrium capacity led the breakthrough to occur quicker as it is shown in **Figure 12 (a)**. From the temperature curves in **Figure 12 (b)**, it is visible that the peak became narrower and decayed faster when moving from $h_w=4.5$ to 9.5 W/m²K, promoted by a higher cooling rate by surrounding. For the adiabatic case, temperature peak was much larger and was retained for a longer period, as illustrated by **Figures 13 (a,b,c)** that shows axial of distribution of temperature for each case inside the column, as the breakthrough front reached the column midway. It is apparent in the adiabatic case that since the heat could not be dissipated through the wall, it was dispersed through the flow and associated with a desorption of CO₂ at reduced equilibrium capacity at peak regions of elevated temperatures.

The Impact of the heat transfer coefficient of the wall in Figure 13 enabled discrimination of the thermal dissipation over the wall from that by gas flow convection in the PBA. High values of heat transfer coefficient of the wall in Figure 11 reduced the hot zone area at the centre of the bed principally by radial cooling, less resistance to heat transfer at the vicinity of the wall and improved mixing over the larger porosity zones in the vicinity of the wall. The reduced

hot zones started from particles with no contact with the wall and cooled off progressively towards the wall. The spatial distribution of energy released from the exothermic adsorption of CO₂ was then the result of improved radial distribution of the heat but also of more complex interplay between the fluid flow as contributor to the heat transfer coefficient of the wall, heat and mass transport rates between zeolite particles and inside zeolite particles. As the adsorption progressed along the bed, the later cooled down, particularly at high values of heat transfer coefficient.



Figures 12 Breakthrough mole fraction (Y_{out}) (a) and temperature (b) profiles for CO₂ as a function of the thermal exchange with the surrounding. PBA of 25 mm ID, 300 mm length, $D_{i,s}=1 \times 10^{-7}$ m²/s, AR of 5, feed inlet velocity of 0.096 m, inlet mole fraction of CO₂ of 0.15 and inlet temperature of 20°C

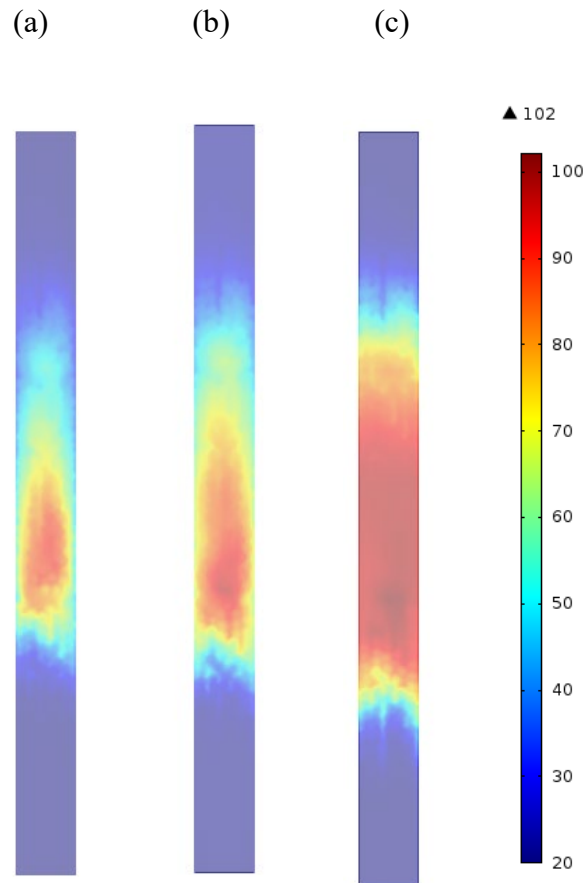


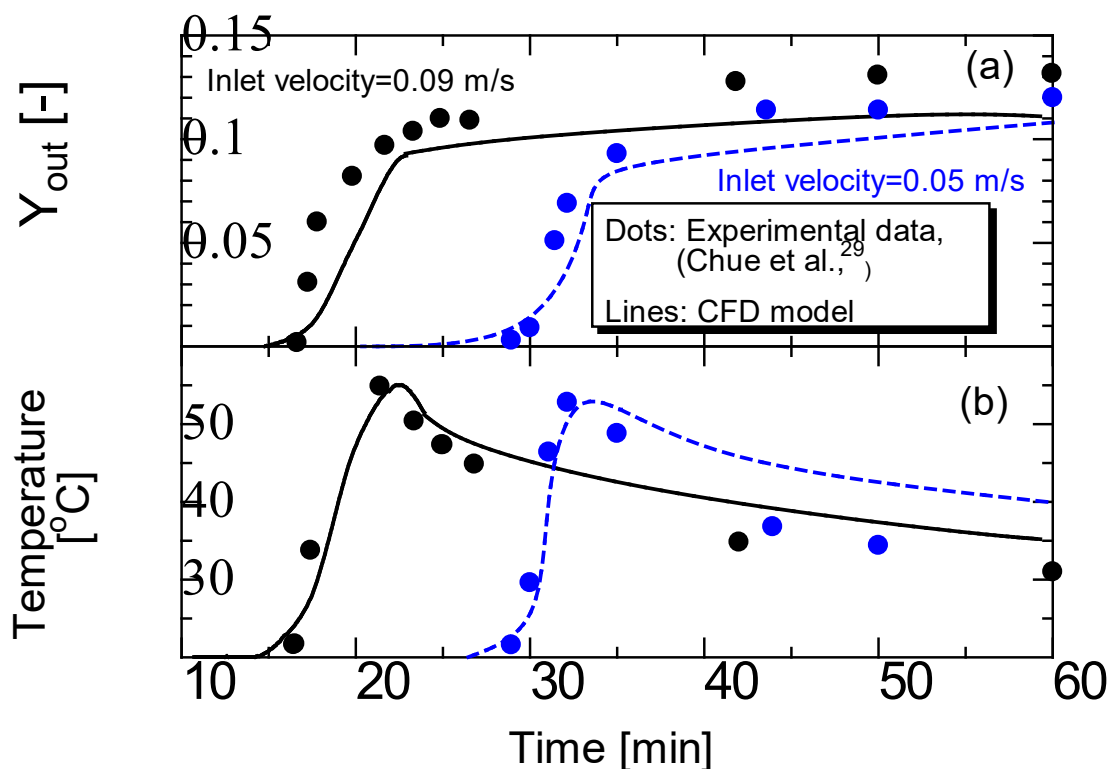
Figure 13 Axial sections of temperature for CO₂ adsorption on zeolite 13X along the PBA at $t=25$ min for (a) $h_w=9.5\text{W/m}^2\text{K}$, (b) $h_w=4.5\text{W/m}^2\text{K}$ and (c) $h_w=0\text{W/m}^2\text{K}$ (right). PBA of 25 mm ID, 300 mm length, $D_{i,s}=1\times 10^{-7}$ m²/s, AR of 5, time of 25 min, feed inlet velocity of 0.096 m, inlet mole fraction of CO₂ of 0.15 and inlet temperature of 20⁰C

2.3 Model validation

The data of isotherms, breakthrough and operating conditions (i.e., including bed length, diameter, porosity, inlet gas velocity, vessel pressure and composition), as illustrated in Table 3, were obtained from the experimental work by Chue et al.²⁹, including an AR of 10 (i.e., 10490 solid particles) and similar volumetric space velocity value of 0.55 and 0.86 h⁻¹ (i.e., inlet velocity of 0.09 and 0.05 m/s, respectively). **Figures 14 (a, b)** show mole fraction breakthrough and temperature for both the experimental study by Chue et al.²⁹ and for the 3D model. The results show similar trends and can be observed to imitate the experimental study, offering access to the key trends in a transient adsorption at local space. The experimental

results showed some differences, most notably the peak temperature and the height of the breakthrough plateau. A reliable data on the physical properties of the PBA (Table 1) along with a more realistic structure that replicate the adsorption of CO₂ would have improved the trends of the dispersive flow (i.e. tails of the curves) observed in Figures 14 (a,b).

The profiles of mole fractions and temperature along the bed length, as shown in Figures 15 (a) and (b), respectively, confirm the key role of heat and mass transfer behaviours during the adsorption process. Unlike differences in temperature between the gaseous phase and the pore of zeolites, those of mole fraction of CO₂ between the gaseous phase and the pore of zeolites, as well as inside the pores, are significant, highlighting relevance of both convective and diffusive mass transfers for this case study.



Figures 14 Validation of the breakthrough mole fraction (Y_{out}) (a) and temperature (b) profiles of CO₂ on zeolite 13X. PBA of 25 mm ID, 100 mm length, diffusivity of 10^{-8} m²/s, AR of 10, Inlet temperature=20⁰C and h_w of 9.5 W/m²K

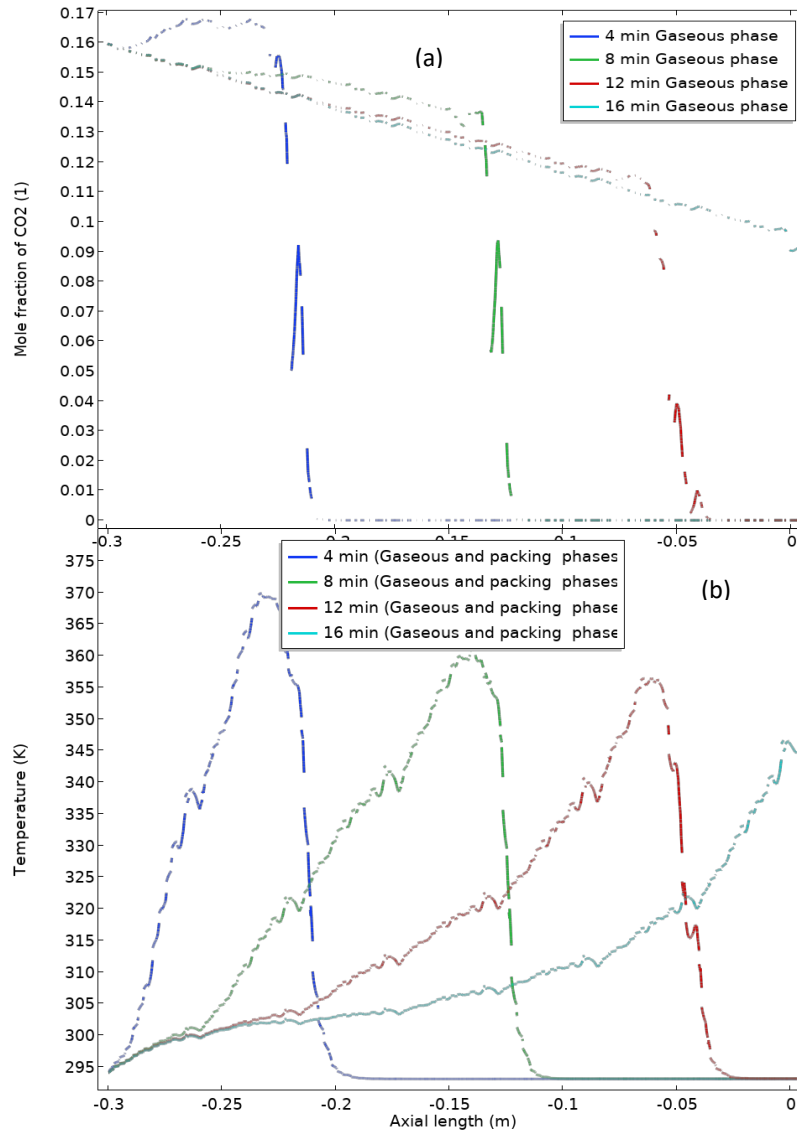


Figure 15 Transient profiles of axial mole fraction of CO₂, Y [-], (a) and temperature (b) along the PBA. Feed inlet velocity of 0.09 m/s and $D_{i,s CO_2}$ of 10^{-8} m²/s, length, AR of 10, inlet mole fraction of CO₂ of 0.15, inlet temperature of 20⁰C and h_w of 9.5 W/m²K

Table 3: Operation characteristics of the PBA

	This work	Xue ²⁷
Inlet velocity (m/s)	0.05-0.095	0.132-0.200
Bed diameter (m)	0.025	0.0254
Bed porosity (-)	0.5	0.32
Length (m)	0.3	1
Zeolite loading (kg)	0.221	0.38
Effective diffusivity (m ² /s)	10^{-8}	10^{-8}
Surrounding and inlet temperature (K)	293	295
Particle size (m)	2.5×10^{-3}	2.5×10^{-3}
Bed density (kg/m ³)	750	750
Heat capacity of zeolite (J/kg.K)	920	920
Operated pressure (kPa)	110	109.4-122.6
Inlet CO ₂ mole fraction (-)	0.15	0.1486
Wall heat transfer coefficient (W/K.m ²)	9.5	7.5-9.5

Conclusion

The use of tube bundle type of adsorbers is highly prominent in current industries of air filters, pollutant control, thermochemical energy storage systems and atmospheric revitalization of confined spaces. The tube bundle type of adsorbers as technology for large scale adsorbers such as CO₂ separations is promising technology, being facilitated by the linear scaleup via numbering up of the tubes of low AR. The modelling of such thin tubes remains not fully certain because of the experimental constraints on access to local changes in flow, temperature, and concentration. In this work, the focus has been to approach the modelling of CO₂ adsorption in discrete porous media using 3D structure and DEM method to reproduce as close as possible the realistic operations. Typical PBA are designed with a reduced mean to reach local adsorption, leading to unpredicted effectiveness distribution along the bed length and oversized approximations to deal with potential uncertainties.

It has been herein possible to access the inside of the PBA during a transient operation mode and helped understanding the local breakthrough phenomena without need of dispersion models which are generally reliable for dedicated laboratory conditions and uniform mixing characteristics. The simulation was set up to minimise use of the empirical parameters and operate a model that represents as close as possible realistic cases. This was done by adopting an adsorption model that relied only on the equilibrium data (isotherms) and driving forces that relied on mass and heat transfers in the solid and gaseous phases and the boundaries of both. The point at which approximations were made was with the lumping of intraparticle parameters which can be approached further by a distinct multiscale approach. An approach that includes intraparticle representation of the pore network as close as possible to the realistic textural geometry that reduces use of the averaging approach by the pore network models.

The CO₂ diffusivity inside the porous zeolite has been investigated over the variation in adsorbent pore size which in turn affects the transport within the solids. The study confirmed any increase in diffusivity would result in a slow onset of breakthrough, widened mass transfer zone and prolonged adsorption taking place. Many of the recently developed materials for enhanced adsorption have been focusing on increasing access to the internal pores and tuning pore geometry for increased mobility and selectivity. The results validated literature knowledge on impact of the diffusion in solids by inhibiting the onset of breakthrough, widening the MTZ and reducing the breakthrough temperature.

The results of the work showed agreement with the experimental results and contributed to access to insight into the behaviours that occur inside the PBA, particularly for long breakthrough time, which was deemed satisfactory as behaviour and the trends were the primary focus. Despite this, there is a great deal of room for further investigation into modelling adsorption in packed beds designed as close as possible to the industrially relevant scales by extension to a tube bundle, actual scaling up of the PBA, reduced approximations of heat and mass transfer at gas-solid boundaries, including both the wall as well as the packing, reduced averaging the solid zeolite structural properties, and dynamic operations under pressure or temperature swinging cycles.

Acknowledgment

The authors would like to acknowledge the support for funding provided by the EPSRC EP/X525583/1.

Abbreviations

a : Ratio of pore surface area to pore volume [$\text{m}^2 \text{m}^{-3}$]

B : Langmuir isotherm parameter [$1/\text{Pa}$]

C_p : Heat capacity [$\text{J kg}^{-1} \text{K}^{-1}$]

c_i : Concentration of species i [mol m^{-3}]

d_p : Particle diameter [m]
 D : Tube wall diameter [m]
 D_i : Diffusivity [$\text{m}^2 \text{s}^{-1}$]
 D_{iK} : Knudsen type diffusion coefficient [$\text{m}^2 \text{s}^{-1}$]
 D_{ib} : Bulk solid type diffusion coefficient [$\text{m}^2 \text{s}^{-1}$]
 h : Heat transfer coefficient [$\text{W m}^{-2} \text{K}^{-1}$]
 I : identity matrix [-]
 k : thermal conductivity [$\text{W m}^{-1} \text{K}^{-1}$]
 M : Molecular weight [kg mol^{-1}]
 p_i : partial pressure of species i [Pa]
 q : adsorbed surface quantity [mol kg^{-1}]
 q_s : Surface saturation quantity [mol kg^{-1}]
 R : universal gas constant [$\text{J mol}^{-1} \text{K}^{-1}$]
 $R_{\text{ads},i}$: rate of adsorption [$\text{mol m}^{-2} \text{s}^{-1}$]
 r_p : average radius pore [m]
 S : Surface area per unit mass [$\text{m}^2 \text{kg}^{-1}$]
 t : time [s]
 T : temperature (K)
 u : velocity vector [m s^{-1}]
 Y : Mole fraction [-]

Greek Letters

ϵ_s : Zeolite porosity [-]
 ΔH_{ads} : Enthalpy of adsorption [J mol^{-1}]
 μ : dynamic viscosity [Pa s]
 ρ : Density (kg m^{-3})
 τ_s : tortuosity [-]

Subscripts:

ads: adsorption
 s: solid phase
 g: gaseous phase
 Surf: surface
 w: wall

Supporting information. Discretisation assessment; Mov 1. Axial sections of concentration of CO₂ adsorption on zeolite 13X along the PBA; Axial sections of temperature for CO₂ adsorption on zeolite 13X along the PBA.

References

- (1) Geden, O.; Peters, G. P.; Scott, V. Targeting Carbon Dioxide Removal in the European Union. *Clim. Policy* **2019**, *19* (4), 487–494. <https://doi.org/10.1080/14693062.2018.1536600>.
- (2) Knox, J. C.; Ebner, A. D.; LeVan, M. D.; Coker, R. F.; Ritter, J. A. Limitations of Breakthrough Curve Analysis in Fixed-Bed Adsorption. *Ind. Eng. Chem. Res.* **2016**, *55*

- (16), 4734–4748. <https://doi.org/10.1021/acs.iecr.6b00516>.
- (3) Sircar, S. Adsorbate Mass Transfer into Porous Adsorbents – A Practical Viewpoint. *Sep. Purif. Technol.* **2018**, *192* (May 2017), 383–400. <https://doi.org/10.1016/j.seppur.2017.10.014>.
- (4) Ma, Q.; Chen, Z.; Liu, H. Multiple-Relaxation-Time Lattice Boltzmann Simulation for Flow, Mass Transfer, and Adsorption in Porous Media. *Phys. Rev. E* **2017**, *96* (1), 013313. <https://doi.org/10.1103/PhysRevE.96.013313>.
- (5) European Commission. Research & Innovation. Literature Review in the Development and Application of Adsorbents for CO₂ Capture. *Eur. Comm.* **2020**.
- (6) Wang, X.; Zhang, F.; Li, L.; Zhang, H.; Deng, S. Carbon Dioxide Capture. In *Advances in Chemical Engineering*; 2021; Vol. 58, pp 297–348. <https://doi.org/10.1016/bs.ache.2021.10.005>.
- (7) Siriwardane, R. V.; Shen, M.-S.; Fisher, E. P.; Losch, J. Adsorption of CO₂ on Zeolites at Moderate Temperatures. *Energy & Fuels* **2005**, *19* (3), 1153–1159. <https://doi.org/10.1021/ef040059h>.
- (8) Esikiewicz-Puchalska, G.; Zgrzebnicki, M.; Michalkiewicz, B.; Kałamaga, A.; Narkiewicz, U.; Morawski, A.W.; Wroble, R. Changes in Porous Parameters of the Ion Exchanged X Zeolite and Their Effect on CO₂ Adsorption. *Molecules* **2021**, *26*, 7520. <https://doi.org/10.3390/molecules26247520>
- (9) Zhao, H.; Wang, Z.; Li, Q.; Wu, T.; Zhang, M.; Shi, Q. Water sorption on composite material "zeolite 13X modified by LiCl and CaCl₂". *Microporous and Mesoporous Materials* **2020**, *299*. 110109, <https://doi.org/10.3390/molecules26247520>
- (10) Bart, H. J.; Germerdonk, R.; Ning, P. Two-Dimensional Non-Isothermal Model for Toluene Adsorption in a Fixed-Bed Adsorber. *Chem. Eng. Process. Process Intensif.* **1996**, *35* (1), 57–64. [https://doi.org/10.1016/0255-2701\(95\)04114-1](https://doi.org/10.1016/0255-2701(95)04114-1).
- (11) Kwapinski, W.; Winterberg, M.; Tsotsas, E.; Mewes, D. Modeling of the Wall Effect in Packed Bed Adsorption. *Chem. Eng. Technol.* **2004**, *27* (11), 1179–1186. <https://doi.org/10.1002/ceat.200407001>.
- (12) Augier, F.; Idoux, F.; Delenne, J. Y. Numerical Simulations of Transfer and Transport Properties inside Packed Beds of Spherical Particles. *Chem. Eng. Sci.* **2010**, *65* (3), 1055–1064. <https://doi.org/10.1016/j.ces.2009.09.059>.
- (13) Dantas, T. L. P.; Luna, F. M. T.; Silva Jr, I. J.; Torres, A. E. B.; de Azevedo, D. C. S.; Rodrigues, A. E.; Moreira, R. F. P. M. Modeling of the Fixed - Bed Adsorption of Carbon Dioxide and a Carbon Dioxide - Nitrogen Mixture on Zeolite 13X. *Brazilian J. Chem. Eng.* **2011**, *28* (3), 533–544. <https://doi.org/10.1590/S0104-66322011000300018>.
- (14) Petrovic, B.; Gorbounov, M.; Masoudi Soltani, S. Influence of Surface Modification on Selective CO₂ Adsorption: A Technical Review on Mechanisms and Methods. *Microporous Mesoporous Mater.* **2021**, *312*, 110751. <https://doi.org/10.1016/J.MICROMESO.2020.110751>.
- (15) Siriwardane, R. V.; Shen, M. S.; Fisher, E. P.; Poston, J. A. Adsorption of CO₂ on Molecular Sieves and Activated Carbon. *Energy and Fuels* **2001**, *15* (2), 279–284. <https://doi.org/10.1021/ef000241s>.
- (16) Wang, Q.; Luo, J.; Zhong, Z.; Borgna, A. CO₂ Capture by Solid Adsorbents and Their Applications: Current Status and New Trends. *Energy Environ. Sci.* **2011**, *4* (1), 42–55. <https://doi.org/10.1039/C0EE00064G>.
- (17) Onyestyák, G. Comparison of Dinitrogen, Methane, Carbon Monoxide, and Carbon Dioxide Mass-Transport Dynamics in Carbon and Zeolite Molecular Sieves. *Helv. Chim. Acta* **2011**, *94* (2), 206–217. <https://doi.org/10.1002/hlca.201000204>.
- (18) Hu, X.; Mangano, E.; Friedrich, D.; Ahn, H.; Brandani, S. Diffusion Mechanism of CO₂

- in 13X Zeolite Beads. *Adsorption* **2014**, *20* (1), 121–135. <https://doi.org/10.1007/s10450-013-9554-z>.
- (19) Silva, J. A. C.; Schumann, K.; Rodrigues, A. E. Sorption and Kinetics of CO₂ and CH₄ in Binderless Beads of 13X Zeolite. *Microporous Mesoporous Mater.* **2012**, *158*, 219–228. <https://doi.org/10.1016/j.micromeso.2012.03.042>.
- (20) Alzahrani, F.; Rusi, H.; Assabumrungrat, S.; Fernandes, D. L. A.; Aiouache, F. Deactivation of the Preferential Oxidation of CO in Packed Bed Reactor by 3D Modelling and Near-Infrared Tomography. *Chem. Eng. J.* **2019**, *378* (June), 122082. <https://doi.org/10.1016/j.cej.2019.122082>.
- (21) Alzahrani, F.; Aldehani, M.; Rusi, H.; McMaster, M.; Abreu Fernandes, D. L.; Assabumrungrat, S.; Nic An tSaoir, M.; Aiouache, F. Gas Flow Visualization in Low Aspect Ratio Packed Beds by Three-Dimensional Modeling and Near-Infrared Tomography. *Ind. Eng. Chem. Res.* **2015**, *54* (51), 12714–12729. <https://doi.org/10.1021/acs.iecr.5b02635>.
- (22) Giese, M.; Rottschäfer, K.; Vortmeyer, D. Measured and Modeled Superficial Flow Profiles in Packed Beds with Liquid Flow. *AIChE J.* **1998**, *44* (2), 484–490. <https://doi.org/10.1002/aic.690440225>.
- (23) Zou, R. ; Yu, A. B. The Packing of Spheres in a Cylindrical Container: The Thickness Effect. *Chem. Eng. Sci.* **1995**, *50* (9), 1504–1507. [https://doi.org/10.1016/0009-2509\(94\)00483-8](https://doi.org/10.1016/0009-2509(94)00483-8).
- (24) He, W.; Lv, W.; Dickerson, J. H. Gas Diffusion Mechanisms and Models; Springer, Cham, 2014; pp 9–17. https://doi.org/10.1007/978-3-319-09737-4_2.
- (25) Schieferstein, E.; Heinrich, P. Diffusion Coefficients Calculated for Microporous Solids from Structural Parameters Evaluated by Fractal Geometry. *Langmuir* **1997**, *13* (6), 1723–1728. <https://doi.org/10.1021/la960889q>.
- (26) Chen, L.; Pannala, S.; Broekhuis, R.; Gautam, P.; Gu, T.; West, D.; Balakotaiah, V. Three-Dimensional CFD Simulation of Pattern Formation in a Shallow Packed-Bed Reactor for Oxidative Coupling of Methane. *Chem. Eng. J.* **2020**, *400* (June), 125979. <https://doi.org/10.1016/j.cej.2020.125979>.
- (27) Qasem, N. A. A.; Ben-Mansour, R. Energy and Productivity Efficient Vacuum Pressure Swing Adsorption Process to Separate CO₂ from CO₂/N₂ Mixture Using Mg-MOF-74: A CFD Simulation. *Appl. Energy* **2018**, *209* (July 2017), 190–202. <https://doi.org/10.1016/j.apenergy.2017.10.098>.
- (28) Pachulski, A.; Schödel, R.; Claus, P. Kinetics and Reactor Modeling of a Pd-Ag/Al₂O₃ Catalyst during Selective Hydrogenation of Ethyne. *Appl. Catal. A Gen.* **2012**, *445–446*, 107–120. <https://doi.org/10.1016/j.apcata.2012.08.018>.
- (29) Chue, K. T.; Kim, J. N.; Yoo, Y. J.; Cho, S. H.; Yang, R. T. Comparison of Activated Carbon and Zeolite 13X for CO₂ Recovery from Flue Gas by Pressure Swing Adsorption. *Ind. Eng. Chem. Res.* **1995**, *34* (2), 591–598. <https://doi.org/10.1021/ie00041a020>.
- (30) LeVan, M. D.; Vermeulen, T. Binary Langmuir and Freundlich Isotherms for Ideal Adsorbed Solutions. *J. Phys. Chem.* **1981**, *85* (22), 3247–3250. <https://doi.org/10.1021/j150622a009>.
- (31) Do, D. D. Fundamentals of Diffusion and Adsorption in Porous Media; 1998; Vol. 2, pp 337–414. https://doi.org/10.1142/9781860943829_0007.
- (32) Celik, I. B.; Ghia, U.; Roache, P. J.; Freitas, C. J.; Coleman, H.; Raad, P. E. Procedure for Estimation and Reporting of Uncertainty Due to Discretization in CFD Applications. *J. Fluids Eng.* **2008**, *130* (7), 078001. <https://doi.org/10.1115/1.2960953>.
- (33) Vortmeyer, D.; Schuster, J. Evaluation of Steady Flow Profiles in Rectangular and Circular Packed Beds by a Variational Method. *Chem. Eng. Sci.* **1983**, *38* (10), 1691–

1699. [https://doi.org/10.1016/0009-2509\(83\)85026-X](https://doi.org/10.1016/0009-2509(83)85026-X).
- (34) Steuten, B.; Pasel, C.; Luckas, M.; Bathen, D. Trace Level Adsorption of Toxic Sulfur Compounds, Carbon Dioxide, and Water from Methane. *J. Chem. Eng. Data* **2013**, *58* (9), 2465–2473. <https://doi.org/10.1021/je400298r>.
- (35) Mangun, C. L.; Daley, M. A.; Braatz, R. D.; Economy, J. Effect of Pore Size on Adsorption of Hydrocarbons in Phenolic-Based Activated Carbon Fibers. *Carbon N. Y.* **1998**, *36* (1–2), 123–129. [https://doi.org/10.1016/S0008-6223\(97\)00169-3](https://doi.org/10.1016/S0008-6223(97)00169-3).
- (36) Massman, W. J. A Review of the Molecular Diffusivities of H₂O, CO₂, CH₄, CO, O₃, SO₂, NH₃, N₂O, NO, and NO₂ in Air, O₂ and N₂ near STP. *Atmos. Environ.* **1998**, *32* (6), 1111–1127. [https://doi.org/10.1016/S1352-2310\(97\)00391-9](https://doi.org/10.1016/S1352-2310(97)00391-9).
- (37) Verma, N.; Mewes, D. Simulation of Temperature Fields in a Narrow Tubular Adsorber by Thermal Lattice Boltzmann Methods. *Chem. Eng. Sci.* **2008**, *63* (17), 4269–4279. <https://doi.org/10.1016/j.ces.2008.05.040>.
- (38) Salem, K.; Kwapinski, W.; Tsotsas, E.; Mewes, D. Experimental and Theoretical Investigation of Concentration and Temperature Profiles in a Narrow Packed Bed Adsorber. *Chem. Eng. Technol.* **2006**, *29* (8), 910–915. <https://doi.org/10.1002/ceat.200600049>.
- (39) Griesinger, A.; Spindler, K.; Hahne, E. Measurements and Theoretical Modelling of the Effective Thermal Conductivity of Zeolites. *Int. J. Heat Mass Transf.* **1999**, *42* (23), 4363–4374. [https://doi.org/10.1016/S0017-9310\(99\)00096-4](https://doi.org/10.1016/S0017-9310(99)00096-4).
- (40) Dirar, Q. H.; Loughlin, K. F. Intrinsic Adsorption Properties of CO₂ on 5A and 13X Zeolite. *Adsorption* **2013**, *19* (6), 1149–1163. <https://doi.org/10.1007/S10450-013-9543-2/TABLES/10>.

Graphical abstract

